Chapter 3

Image potential state dynamics of electrons at Cu(100)

3.1 Introduction

At a metal surface two types of electronic states can be found which don't exists in a bulk metal. These states are intrinsic surface states and image potential states, respectively. They differ in their charge density localization relative to the surface. Intrinsic surface states are more or less localized at the surface atomic layer. The existence of these states was predicted theoretically by Tamm [73] and Shockley [74]. Image potential states are localized mostly in the vacuum region. They were predicted by Echenique and Pendry [75] and found experimentally by inverse photoemission experiments a few years later [76, 77].

The concept of image potential states is quite easy to understand. An electron in front of a conducting metal surfaces moves in a Coulomb like attractive image potential [78], which can be idealized as

$$V(z) = -\frac{e^2}{4z} \quad . \tag{3.1}$$

The potential [in Eq. (3.1) we use units in which $4\pi\epsilon_0 = 1$] is created by the electron interacting with a positive image charge at the same distance

z inside the solid (see Fig. 3.1). An electron, transferred from the bulk for instance by a laser, can be trapped in this attractive potential at the surface. The trapping time can be considerably long if the metal has a projected band gap along z (the surface normal) in the relevant energy region near the vacuum energy ($E_{vac} = 0$) where the image charge states are situated. The eigenstates of the trapped electron then form a hydrogen like Rydberg series with energies E_n [79]

$$E_n = \frac{-A}{(n+a)^2} \qquad . \tag{3.2}$$

In principle there is an infinite number of image potential states with energies E_n converging towards the vacuum energy. In Eq. (3.2) the influence of the metal surface on E_n is modeled in an approximate fashion by a quantum defect a in analogy to the treatment of an alkali atom, for example, in atomic physics. For the most metal surfaces investigated to date, a is in the range $0 \leq a \leq 0.5$. For the simplest model with an infinite surface barrier these states should have an infinite lifetime, and the constant A in Eq. (3.2) is then 1/16 of a Rydberg, *i.e.*, $A = 0.85$ eV. In a real system the trapped electron couples to the electronic degrees of freedom inside the metal, *i.e.*, electron-hole pairs are created for example, and the electron decays back into the metal after a finite time. Because the image charge wave functions are almost completely localized outside the surface (see below), the lifetimes are in many cases significantly longer than those of electronic excitations inside the metal [78]. In particular high-lying states can "live" for many picoseconds.

Image potential states are very useful model systems for a systematic investigation of the electron dynamics at surfaces including energy and phase relaxation effects due to the "non rigidity" of the surface.

There have been many theoretical calculations (based on models or first principles) to obtain the energies of image potential states (see for example Refs. [75, 79, 80, 81, 82, 83, 84, 85, 86, 87, 88] or [89], and references therein). The theoretical calculation of lifetimes for image potential states has also attracted much interest. A first and simple estimate, based on the extent

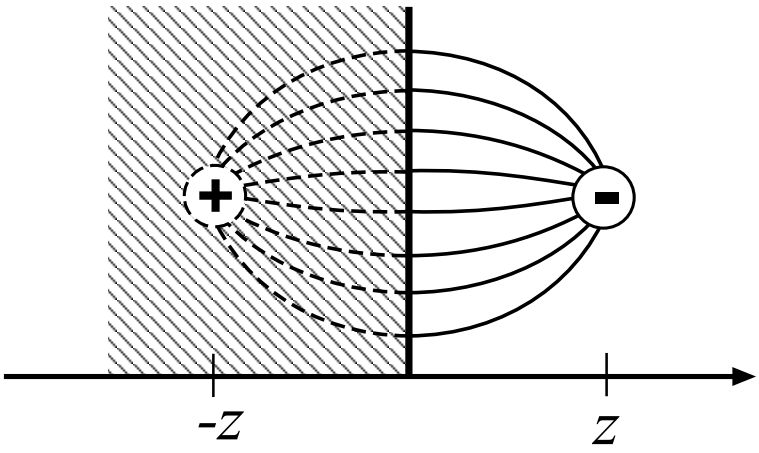

Figure 3.1: Sketch of the electric field lines for an electron at a distance z in front of a conducting metal surface (solid lines). In an idealized picture this field can be explained by assuming the existence of a positive image charge inside the solid at $-z$ (field lines are indicated by dashed lines).

of penetration of the image state wave function into the bulk was given in Ref. [75]. Subsequently more sophisticated scattering calculations within the self-energy formalism were performed (Refs. [90, 91, 92, 93]).

Experimentally image potential states have been intensively examined as well. First by inverse photoemission spectroscopy (see Refs. [94, 95, 96, 80, 97, 98] and later by time-independent Two-Photon-Photo-Emission (2PPE) spectroscopy (Refs. [99, 100] and [101]). The latter is a pump probe type technique which will be described in more detail below. Thanks to these investigations the energies of image potential states for many noble and transition metals are now known. These time-independent experiments, however, were often restricted to the lowest two image potential states due to the limited energy resolution. Also investigations of image-type surface states using tunneling spectroscopy were performed [102]. However, here not the "pure" image states are probed, since the field of the tunneling junction distorts the image potential (3.1) somewhat.

More insight into the nature of image potential states can be obtained by

femtosecond Time-Resolved-Two-Photon-Photo-Emission (TR-2PPE) spectroscopy. With this technique the lifetimes of image potential states can directly be measured in the time domain. By using femtosecond pulses with large spectral width a coherent excitation of several higher image potential states is enforced. Using a probe laser, one can then monitor the electronic wave packet motion in the form of a quantum beat spectrum. In this way the energies of higher lying image states ($n > 2$) become accessible. TR-2PPE experiments have been carried out for various surfaces such as Cu(100) [17, 16, 18], Ag(111) and Ag(100) [103, 104, 105], Cu(111) [106, 107, 108]. More recently, also Angle-Resolved Spectra (AR-TR-2PPE) have been recorded for various, notably stepped surfaces [109]. These give information also on the lateral motion of the electron on the surface.

In this thesis TR-2PPE experiments on a clean Cu(100) surface (Refs. [17, 16, 18]) will be modeled. We use strictly the one electron approximation, neglect lateral motion of the electron (see below), and further consider two cases:

(i) Treatment of the electron dynamics in the image potential states without any dissipative effects by means of the time-dependent Schrödinger equation.

(ii) Solution of the open quantum system Liouville-von Neumann equation, where the interaction with the bulk electrons is treated in a semi-phenomenological way as "dissipation".

These two models will be explained in detail in the next sections. In particular the second example is of the non rigid surface type. The inclusion of finite lifetime effects turns out to be of central importance for the interpretation of the experimental data.

First, let us have a closer look at the experiments themselves [16, 17, 18]. In Fig. 3.2 a sketch is given to illustrate what actually happens during the course of a TR-2PPE experiment. The first step is the excitation of conduction band electrons just below the Fermi energy ($E_{Fermi} \approx -4.6$ eV)

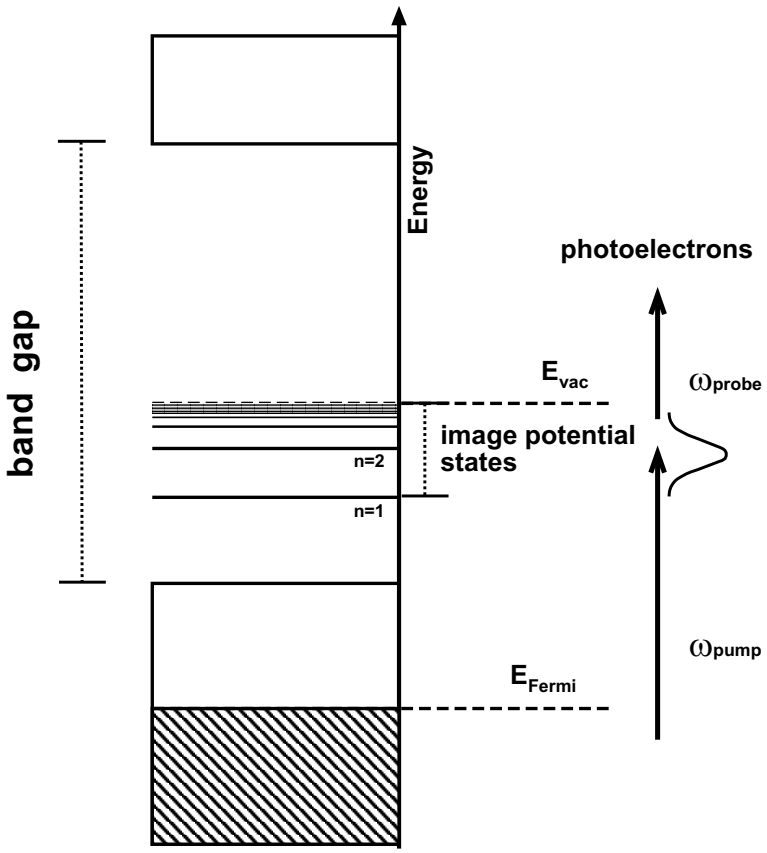

Figure 3.2: Sketch of the 2PPE experiment for Cu(100). On the left side the occupied conduction band states below the Fermi energy are shown, together with the unoccupied conduction band states. For Cu(100) these bulk states below the vacuum level ($E_{vac} = 0$) are separated from a continuum of empty metal states above E_{vac} by a large band gap of $\approx$ 6 eV. Inside the band gap, the "Rydberg" series of the image potential states is situated. First electrons are excited form states below the Fermi energy into image potential states by the pump pulse (ω_{pump}) and after a certain delay time probed as photoelectrons by the probe pulse (ω_{probe}).

into image potential states by a "blue" femtosecond laser pulse of appropriate energy ($\hbar\omega_{pump} = 4.7$ eV). Due to the finite band width of the pump laser pulse, for higher image potential states generally not a pure state but a superposition of many image potential states is excited. After a certain delay time $\Delta\tau$ the electrons inside the image potential are probed by a second "red" femtosecond laser pulse ($\hbar\omega_{probe} = 1.57$ eV) which transfers the electrons in non bonding continuum states above E_{vac}. The ejected photoelectrons are then detected and energy-analyzed according to their kinetic energy E_{kin}.

In these experiments, one has two key parameters leading to two key modes in which the experiment can be carried out. If the pump probe delay $\Delta\tau$ is kept fixed and the photoelectron signal is recorded as a function of the electron kinetic energy E_{kin}, one has an "energy resolved 2PPE" spectrum. If, on the other hand, the signal at a fixed kinetic energy is recorded as a function of the delay time $\Delta\tau$, one obtains a TR-2PPE spectrum. The energy resolved 2PPE spectrum gives information on the energies of the (low-lying) image states, and - through the linewidths - some information on dissipation effects (lifetime and pure dephasing). The time resolved spectra show characteristic, damped "quantum beats". The location of these "beats" contains information on the energy differences between (high-lying) image potential states, while the amount of damping reflects the strength of dissipation.

3.2 Model and eigenstates

3.2.1 Model and potential

In the following, a single electron moving in an effective potential $V(z)$ created by all nuclei and all other electrons will be considered. The eigenfunctions of the electron in the image state potential are centered, in particular for the higher states, far away from the surface (see section 3.2.3). Therefore, at least for low-index surfaces the surface corrugation can be neglected and the electron's 3D wave function can be well approximated by

$$\psi_{n,\underline{k}_\parallel}(\underline{r},z) = N\ e^{i\underline{k}_\parallel \underline{r}}\ \psi_n(z) \quad . \tag{3.3}$$

Here, $\underline{k}_\parallel$ is the electron momentum parallel to the surface [$\underline{r} = (x,y)$], $\psi_n(z)$ is the component of the electronic wave function oriented along the surface normal, and N is a normalization factor. The eigenenergies corresponding to Eq. (3.3) are

$$E_{n,\underline{k}_\parallel} = \frac{\hbar^2 k_\parallel^2}{2m_e} + E_n \quad , \tag{3.4}$$

where the first term stands for the free lateral motion of the electron of mass m_e, and E_n is a quantized energy state describing the motion perpendicular to the surface. In the uncorrugated surface model the entire problem then comes down to finding the eigenstates of the electron moving along z according to

$$\hat{H}_0\psi_n(z) = \left[-\frac{\hbar^2}{2m_e}\frac{d^2}{dz^2} + V(z)\right]\psi_n(z) = E_n\psi_n(z) \quad , \tag{3.5}$$

where $V(z)$ is the effective one electron potential mentioned above. The eigenstates E_n in (3.5) can be classified as (bound and unbound) bulk states and as bound and unbound image charge states, respectively, as will be demonstrated below.

Model potential

To construct the local one electron pseudo potential $V(z)$, a functional form suggested by Chulkov *et al.* [89] in connection with a slab model is used. This potential is parameterized as follows:

$$V_1(z) = A_{10} + A_1 \cos\left(\frac{2\pi}{a_s} \mid z \mid\right), \qquad \mid z \mid < D \tag{3.6}$$

$$V_2(z) = -A_{20} + A_2 \cos\left(\beta(\mid z \mid -D)\right), \qquad D < \mid z \mid < z_1 \tag{3.7}$$

$$V_3(z) = A_3 \exp\left[\alpha\left(\mid z \mid -z_1\right)\right], \qquad z_1 < \mid z \mid < z_{im} \tag{3.8}$$

$$V_4(z) = \frac{\exp\left[\lambda\left(\mid z \mid -z_{im}\right)\right]}{4\left(\mid z \mid -z_{im}\right)}, \qquad z_{im} < \mid z \mid \quad , \tag{3.9}$$

and $V(z) = V_1(z) + V_2(z) + V_3(z) + V_4(z)$, where $V_i(z)$ $(i = 1, ..., 4)$ is set to zero outside the corresponding interval given above. There are only four independent parameters in the model, namely A_{10}, A_1, A_2 and β; further, D is one half of the thickness of the slab which has been chosen to represent the Cu(100) surface. In the following a slab consisting of 601 layers of Cu atoms will be used, each one separated by the lattice constant a_s. In this case, $D = 1024.5\ a_0$. All other parameters are determined by forcing the potential and its first derivative to be continuous. The potential parameters relevant for Cu(100) are shown in Table 3.1. The first term of the potential [Eq. (3.6)] describes the bulk potential which is terminated at the two surface atomic layers at $z = \pm D$ which exist in a slab model. The parameters A_{10} and A_1 have been fitted to the experimental width and position of the energy gap, respectively [89]. Eqs. (3.8) and (3.7) model the solid-vacuum interface region with a smooth transition towards a pure screened Coulomb potential [Eq. (3.9)] for large distances from the surface layer. In Eq. (3.7) the parameters A_2 and β were determined to fit the energies of the first image potential state or the surface state [89].

The parameters determined in Ref. [89] accurately reproduce results form density functional theory, and key features such as the band gap and binding energies of the image potential states. In Fig. 3.3 the potential around the surface region of Cu(100) is given with a graphic illustration of some of

(a) Independent parameters

$a_s(a_0)$	A_{10}(eV)	A_1 (eV)	A_2(eV)	$\beta(a_0^{-1})$
3.415	-11.480	6.10	3.7820	2.5390

(b) Other parameters

$z_1(a_0)$	A_{20}(eV)	A_3 (eV)	$\alpha(a_0^{-1})$	$\lambda(a_0^{-1})$	$z_{im}(a_0)$
1.54667	9.162	-11.8363	0.573659	1.14732	2.27253

Table 3.1: Potential parameters for Cu(100) from Ref. [89]. (a) gives the independent parameters (b) the remaining parameters calculated by demanding the potential and its first derivative to be continuous in z. Note that z_1 and z_{im} are given relative to the surface atomic layer at $z = 0$. Their actual value in Eqs. (3.8) and (3.9) depends on D and therefore on the number of atomic layers in the Cu slab.

the potential parameters. Interestingly, for this potential the image plane position (z_{im}) is obtained automatically, from the values of A_{10}, A_1, A_2 and β. Fig. 3.5 (a) below shows the potential curve $V(z)$ over the full range of z values (from $\approx -4500\ a_0$ to $\approx +4500\ a_0$) that was actually used in the calculation with the 601 layer slab.

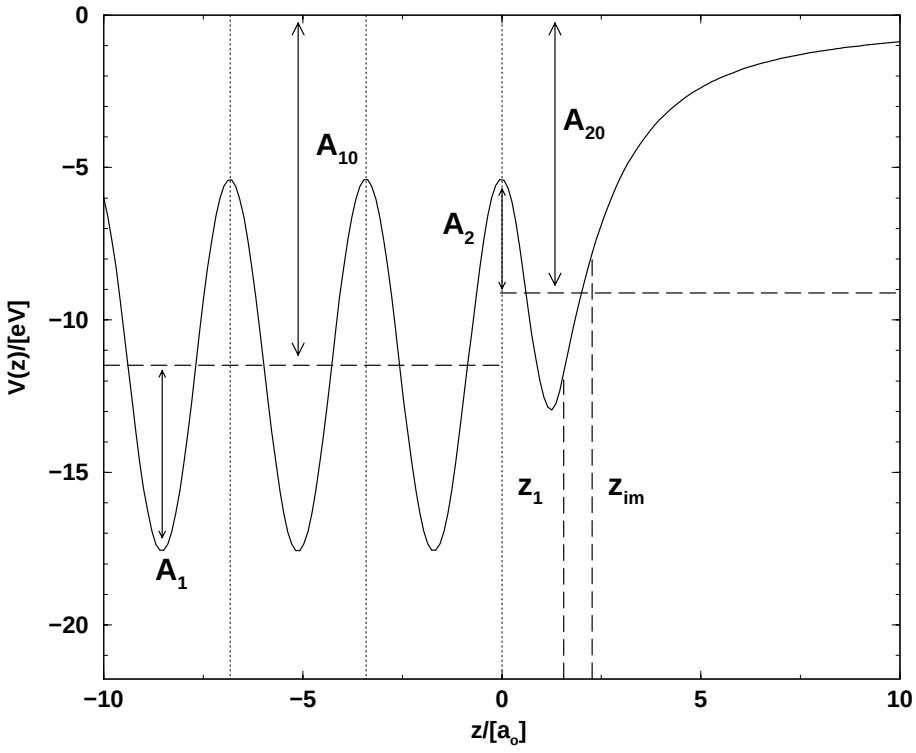

Figure 3.3: The one dimensional effective potential used for electrons at Cu(100) near the surface atomic layer (which was placed here for convenience at $z = 0$). The dotted lines indicate the atomic layer positions. Values of certain potential parameters are indicated by dashed lines and arrows, respectively.

3.2.2 Evaluation of eigenstates: The mapped Fourier grid method

Since all dynamical calculations below to simulate 2PPE spectra will be performed in an eigenstate basis, the next step is the evaluation of the electronic eigenfunctions $\psi_n(z)$ for the potential used, *i.e.*, the solution of Eq. (3.5). These eigenfunctions are evaluated with the so called mapped Fourier grid method [110]. The (unmapped) Fourier grid method was originally proposed in Refs. [111], [112], and [113], and further developed in Refs. [114] and [115, 116]. The grid mapping for grid based methods has been employed first in [117] for electronic structure theory. In the following the combination of these methods will be described for the one dimensional problem arising here, but the mapped Fourier grid method can be applied to any dimensionality, for nuclear dynamics [118], and even for explicitly time-dependent problems [119].

Fourier grid methods in general have the advantage of scaling only moderately in their computation time with the number of grid points N, according to $N\log_2 N$ when the Fast Fourier Transform algorithm is used (see Appendix A.1). However, the FFT requires an equidistant grid. In our application the grid point density is determined by the fast variation of $V(z)$ in the bulk and close to the surface, while the potential at greater distances from the surface (where the higher image states are located) is very flat (see Fig. 3.5 (a) below). To avoid too large grid point densities over the whole z range of interest, the mapped Fourier grid method is most useful. By rewriting the kinetic energy operator it becomes possible to use a non equidistant, physical grid, with high density in the bulk and near surface region, while far away from the surface the grid spacing can be chosen quite large. In this way it becomes possible to calculate even very high lying image potential states (up to $n = 15$) which extend thousands of Angstroms into the vacuum, with high accuracy.

To illustrate the mapped Fourier grid method to solve the eigenvalue problem of Eq. (3.5), let us first describe the "ordinary" Fourier grid method.

Here, a grid is defined by points z_i $(i = 1, \ldots, N)$ equally spaced over the coordinate z. Then one can use Dirac δ functions located at those grid points, as a basis to expand any wave function $\psi(z)$:

$$\varphi_i(z) = \delta(z - z_i) \qquad (i = 1, ..., N) \quad . \tag{3.10}$$

Expressed in the basis spanned by the functions (3.10) the kinetic energy operator $\hat{T} = -\frac{\hbar^2}{2m_e^2}\frac{d^2}{dz^2}$ and the potential $V(z)$ become $N \times N$ matrices $\mathbf{T}$ and $\mathbf{V}$. $\mathbf{V}$ is diagonal in coordinate representation, while $\mathbf{T}$ is diagonal in the momentum representation, which is connected by a Fourier transform to the coordinate representation. By using the appropriate Fourier transform one can easily compute the Hamilton matrix $\mathbf{H} = \mathbf{T} + \mathbf{V}$ and diagonalize it to obtain the eigenvalues and corresponding eigenfunctions. Due to the grid representation the minimal de Broglie wavelength and so the maximal kinetic energy that can be represented are determined by the sampling theorem (chapter 12 of Ref. [58]). Accordingly the maximal kinetic energy that can be represented by a grid spacing $\Delta z = z_{i+1} - z_i$ is

$$E_{kin,max} = \frac{1}{2\ m_e} p_{max}^2 \quad , \tag{3.11}$$

where $p_{max} = \frac{\hbar\ \pi}{\Delta z}$. So the grid spacing has to be chosen small enough to resolve the highest momentum included in the desired eigenfunctions. As outlined above, within the bulk and close to the surface the electron can gain a large momentum p_{max} requiring Δz to be small. In contrast, for large z, p_{max} is small and so Δz can be chosen large. Hence, when the FFT algorithm with an equidistant grid is used to transform back and forth between coordinate and momentum space, and when simultaneously the "inner" and the "outer" regions of $V(z)$ are of interest, the number of grid points N becomes prohibitively large. This is a storage problem but also a computation time problem, because the diagonalization of the $N \times N$ Hamilton matrix scales as N^3.

This problem can be circumvented by introducing an equidistant "auxiliary" grid in a new coordinate q which is related to a non equidistant,

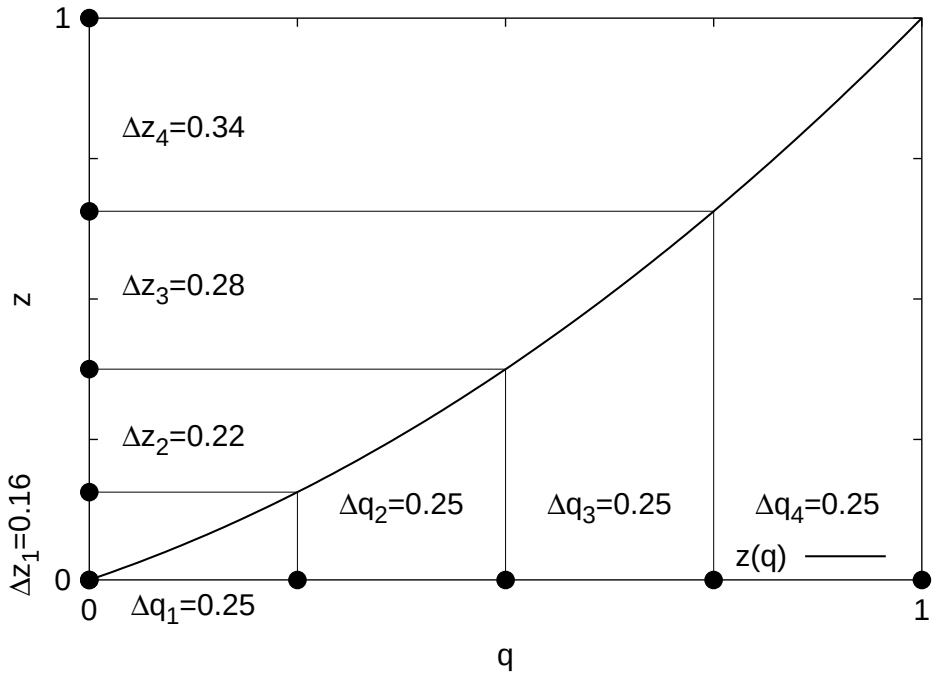

Figure 3.4: Illustrative example for the mapped grid procedure. Here a non equidistant, "physical" grid in z is related to a "auxiliary" grid in q. The grid in q has a constant grid spacing with $\Delta q = 0.25$. The mapping function chosen is $z(q) = \frac{1}{2}(z + z^2)$. One can see that the actual grid spacing in z depends on the derivative of the mapping function [*i.e.*, the steeper the slope of $z(q)$ the larger the local grid spacing in z.]

"physical" grid in z through the mapping function $z(q)$. The physical grid is used to represent the momenta, the auxiliary grid to do the FFT. The mapping procedure is illustrated in Fig. 3.4 for the example of a mapping function $z(q) = \frac{1}{2}(z + z^2)$, and five grid points. One can see that the local physical grid spacing in z depends on the derivative of $z(q)$. A steep slope of $z(q)$ produces a large grid spacing in z, while if $z(q)$ is flat the grid spacing Δz is small.

To apply the mapping procedure, we rewrite the Hamiltonian $\hat{H}_0$ in Eq.

(3.5) as

$$\hat{H}_0 = V(z(q)) - \frac{\hbar^2}{2m_e}\left(\frac{\partial q}{\partial z}\frac{\partial}{\partial q}\right)^2 \quad . \tag{3.12}$$

There are different methods to apply the kinetic part of the Hamilton operator, which differ in the numerical effort and stability (see for example [118]). Here, the most stable one to evaluate $\hat{T}\psi(q)$ is used, which proceeds as follows:

1. Transform $\psi(q)$ to momentum space (by FFT) and apply $\frac{\partial}{\partial q}$, *i.e.*, evaluate $ik_q\psi(k_q)$.

2. Back transform $\psi(k_q)$ (by inverse FFT) and apply $\frac{\partial q}{\partial z}$, *i.e.*, evaluate $\frac{\partial q}{\partial z}\psi(q)$.

3. Repeat step 1.

4. Repeat step 2 and multiply by $\frac{-\hbar^2}{2m_e}$.

The algorithm requires four Fourier transforms to calculate $\mathbf{T}$ instead of two for an equidistant grid in z, but we need much fewer grid points N in the mapped case (see below).

Figure 3.5 shows the potential $V(z)$ (a), the inverse mapping function $q(z)$ (b) and its derivative $\frac{\partial q}{\partial z}$ (c) for the problem at hand. $z(q)$ is evaluated by cubic spline interpolation between 100 points (q, z) which are chosen to reproduce the prespecified grid spacing inside the solid Δz_{solid} and in the image potential region Δz_{vacuum}. The chosen grid parameters are given in Table 3.2. The mapping function and its derivative are inverted numerically. The advantage of this purely numerical approach is that any topology of the mapping function is possible. A disadvantage is that one encounters oscillations in the derivative [Fig. 3.5 (b)]. However, it was made sure that these oscillations don't affect the accuracy of the calculation.

It can also be seen in Fig. 3.5 that in the slab the potential is symmetric with respect to $z = q = 0$. Therefore the numerical effort can be further reduced by using symmetry adapted basis functions. We can construct $N/2$

$z_{min,max}(a_0)$	$\Delta z_{solid}(a_0)$	$\Delta z_{vacuum}(a_0)$
$\pm$ 4464.2	≈ 0.3	≈ 2.25

Table 3.2: Grid parameters used for evaluation of the electronic eigenstates.

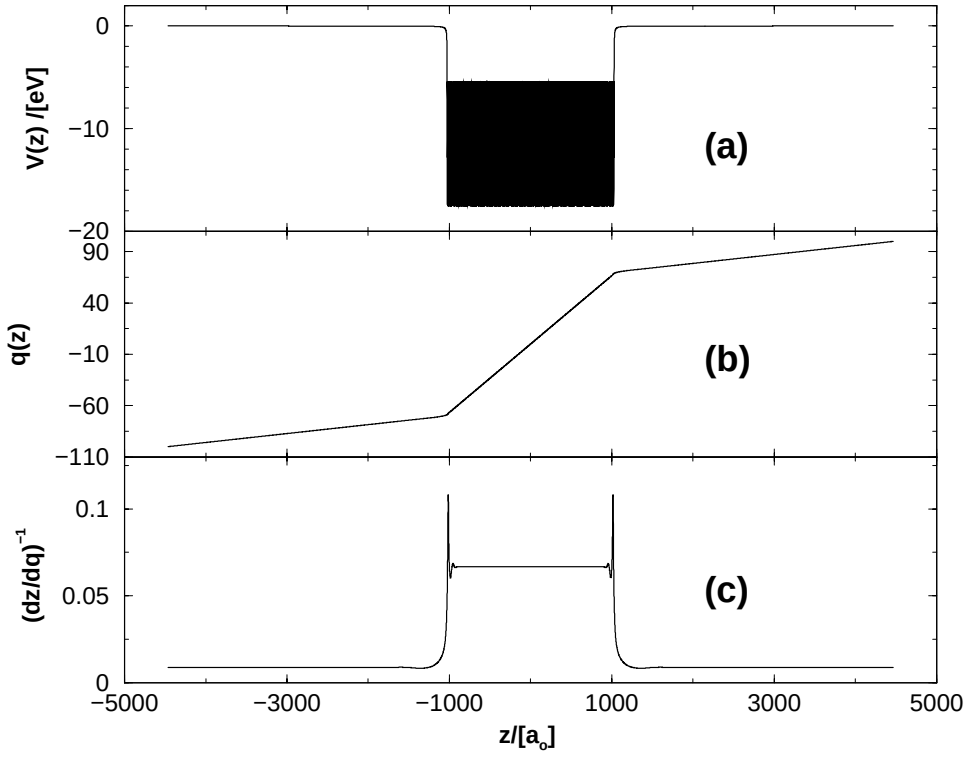

Figure 3.5: Potential $V(z)$ for the electron at Cu(100) (a). In the middle on can see the 601 Cu layers with the vacuum regions attached on both sides. The surface layers are located at $z = \pm D = \pm 1024.5\ a_0$. (b) shows the inverse mapping function $q(z)$ used for evaluation of eigenstates; the derivative $\left(\frac{dz}{dq}\right)^{-1}$ is given in (c). For the *inverse* mapping function a large derivative means a small grid spacing along z (inside the Cu slab and close to the surface), and a small derivative a large grid spacing (for the vacuum regions).

symmetry adapted basis functions of gerade symmetry,

$$\varphi_{i,g}(q) = c\ [\delta(q - q_i) + \delta(q + q_i)] \tag{3.13}$$

and $N/2$ basis functions of ungerade symmetry (u)

$$\varphi_{i,u}(q) = c\,[\delta(q - q_i) - \delta(q + q_i)]\ . \tag{3.14}$$

Here c is the appropriate normalization factor given by the condition

$$\int_{-\infty}^{+\infty} \varphi_{i,k}(q)^* \varphi_{j,l}(q) \frac{\partial z}{\partial q} dq = \delta_{kl}\delta_{ij} \qquad . \tag{3.15}$$

In this basis the elements of the (2×2) block diagonal Hamilton matrix are as follows:

$$H_{(i,k),(j,l)} = \delta_{kl} \int_{-\infty}^{+\infty} \varphi_{i,k}(q)^* \hat{H}_0 \varphi_{j,l}(q) \frac{\partial z}{\partial q} dq \qquad . \tag{3.16}$$

By diagonalizing (3.16) we obtain $\frac{N}{2}$ eigenstates ψ_n^g of gerade (g) symmetry and the corresponding eigenenergies, and $\frac{N}{2}$ ungerade (u) eigenfunctions ψ_n^u and the corresponding energies. The classification of the eigenstates as gerade or ungerade, is due to the slab approach which introduces an inversion center. If the slab thickness is chosen big enough gerade and ungerade states come in (almost) degenerate pairs, and either set (gerade or ungerade eigenstates) or a combination of both can be used as a basis for dynamical calculations with (almost) identical results (see below).

3.2.3 Evaluation of eigenstates: Results

The eigenstates are evaluated in an energy range from ≈ -6.25 to $\approx +2.18$ eV relative to the vacuum energy $E_{vac} = 0$. The eigenvalues for functions of gerade symmetry are given schematically in Figure 3.6. The first 83 states represent bound, bulk electronic states extending up to the upper edge of the conduction band, some of them below, some above the Fermi level at $E_{Fermi} = -4.62$ eV. Then follow the image potential states, located in the band gap of Cu(100), the first 15 of which are shown as an inset in Fig. 3.6.

In principle there is an infinite number of bound states in an Coulomb like potential, but as a discrete grid is used here only a finite number of them can be resolved. Above the image potential states one finds the states corresponding to the unbound continuum typical for a H-like Coulomb potential. Their energies are positive ($> E_{vac}$), and in our discrete numerical approach practically identical to those of a particle in a one dimensional box. In our example the borders of the box are given by the two surface atomic layers, because in the energy range shown the image state continuum wave functions lie in the Cu(100) band gap and practically cannot penetrate into the bulk.

(I) Image states: Wave functions and energies

Let us now investigate the image states in more detail. We denote those by ψ_n, where n is the image state quantum number, starting from $n = 1$. (Note that so far ψ_n has been used for all states supported by $V(z)$ – see (3.5) for example.) Convergence tests showed that the grid chosen accurately determines the eigenenergies of up to $n = 15$. Therefore, in the dynamical calculations (section 3.4) 15 image states will be included. The $n = 15$ image state wave function (of ungerade symmetry) is shown in Fig. 3.7 (a) for illustration. Note that this wave function ψ^u_{15} extends several thousands of Angstroms into the vacuum region! Note also that according to Table 3.2 using a small grid spacing of $\Delta z_{solid} = 0.3a_0$ over the whole z range, representing this wave function would have required a grid consisting of $\approx$ 30000 points. With the mapping procedure we need only 10540 points. In Fig. 3.7 (b) we also show the three lowest image state wave functions (u) ψ^u_1, ψ^u_2, and ψ^u_3. These are much less extended than ψ^u_{15}. In the ideal situation of an infinite surface barrier (pure Coulomb potential), the image charge wave functions are given by the expression

$$\psi_n = N z R_n^{l=0}\left(\frac{z}{4}\right) \quad . \tag{3.17}$$

Here, $R_n^{l=0}$ is the radial part of a ns wave function for a H atom [78] expanded along z (by the argument $z/4$), and N is a normalization factor. The "real"

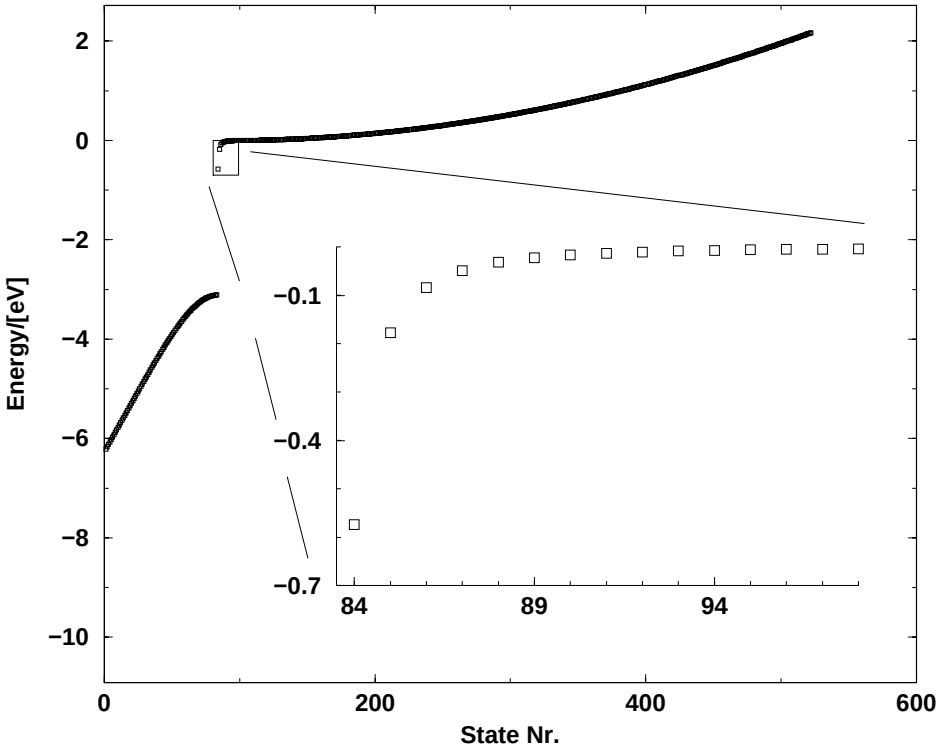

Figure 3.6: Electronic eigenenergies for the Cu(100) model potential $V(z)$ (gerade symmetry only), obtained by solution of the time-independent Schrödinger equation (3.5). The inset shows a magnification or the first 15 image potential states. On the left one can see the upper part of the conduction band. On the right "particle in a box" like continuum energies of the image potential are shown.

wave functions of Fig. 3.7 reflect this behaviour, but show also some important differences. In particular the wave functions penetrate slightly into the bulk region. The amount of penetration is an approximate measure for the lifetime of the respective image states (see below). Quantitatively we calculate the penetration of image state ψ_n into the bulk by

$$p_n = \int_{-z_{im}}^{z_{im}} \mid \psi_n(z) \mid^2 dz \quad . \tag{3.18}$$

Simple considerations [101] suggest that p_n scales approximately with the inverse of the third power of $(n + a)$ (a being again the quantum defect):

$$p_n = d(n + a)^{-3} \quad . \tag{3.19}$$

Hence, the higher image states have a smaller penetration into the bulk. The expectation (3.19) is nicely confirmed out by our numerical experiment which shows a strict linear relationship between $p_n^{-1/3}$ and n (Fig. 3.8), giving $d = 0.11$ and $a = 0.24$.

As suggested by Eq. (3.2) the energies of the image states are approximately (infinite barrier model) inversely proportional to $(n + a)^2$, with $A = 0.85$ eV. In Fig. 3.8 also $\frac{1}{\sqrt{-E_n}}$ is shown as a function of n, confirming excellent agreement with (3.2) with $A = 0.854$ eV and $a = 0.24$.

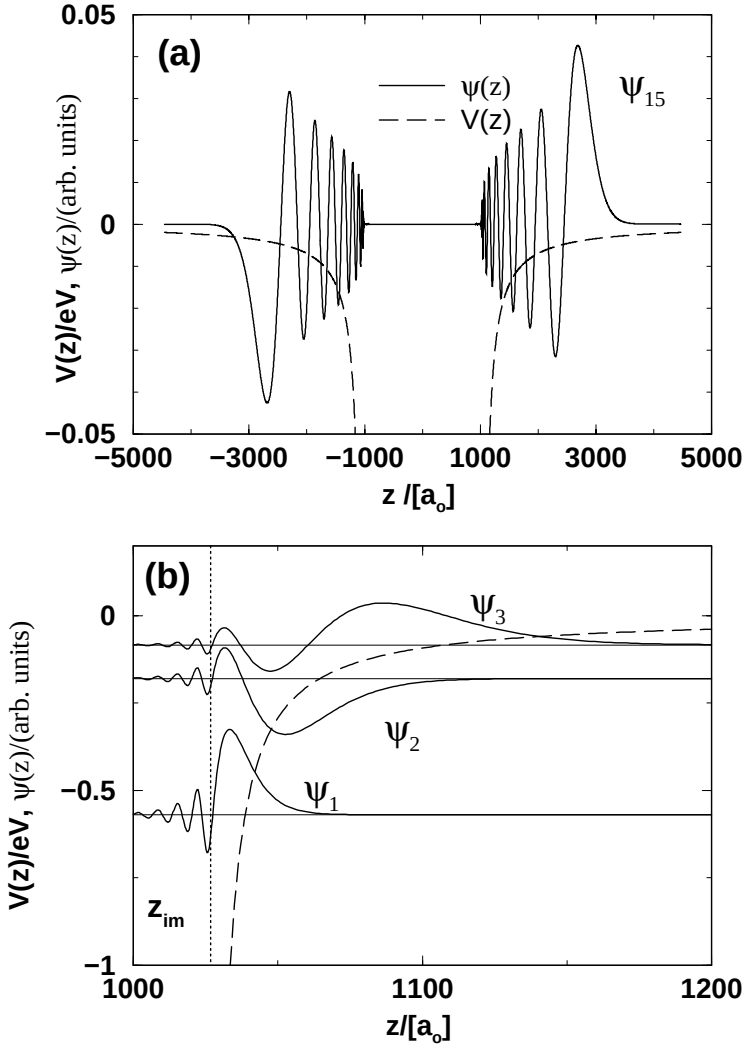

Figure 3.7: (a) Eigenfunction (u) of highest image potential state used in the propagations ($n = 15$). The wave function is shown along the physical coordinate z. Note that ψ^u_{15} is still well placed inside the grid boundaries. (b) The lowest three image states (u). Only the part located around the right surface atomic layer at $z = 1024.5\ a_0$ is shown. Note their similarity to H ns wave functions, and the slight penetration into the bulk region. The dotted line gives the image plane position at $z = 1026.8\ a_0$.

state n	energy $E_n - E_{Fermi}$ (eV)		lifetime τ_n (fs)		
	here	[18]	here	[18]	[120]
1	4.056	4.04	22	40±6	30
2	4.453	4.45	112	120±15	132
3	4.547	4.545	337	300±20	367
4	4.582	4.580	756	630	–
5	4.599	4.598	1431	1200	–
6	4.608	4.608	2423	2000	–

Table 3.3: Image state energies $E_n - E_{Fermi}$ relative to the Fermi energy, and lifetimes τ_n based on the penetration of the wave functions into the bulk. The data of this work ("here") are compared to experimental values [18] and other theoretical calculations [120].

(II) Image states: Lifetimes

Since the image state wave functions penetrate into the bulk [Eq. (3.19)], they can interact with the bulk electrons. This leads to electron-electron scattering processes (electron-hole pair creation), resulting in a finite lifetime τ_n for the image state ψ_n. A simple heuristic formula by which these lifetimes can be evaluated, is [101]:

$$\tau_n = b(E_n - E_{Fermi})\frac{1}{p_n} \tag{3.20}$$

Here p_n is given by Eq. (3.19), and b is a metal specific constant ($b = 0.13\frac{1}{\mathbf{eVs}}$ for Cu [101]).

Table 3.3 compares calculated lifetimes (3.20) for various image states, with those obtained by experiment [18], and by a more sophisticated scattering theoretical approach [120]. Also shown are the energies $E_n - E_{Fermi}$ and compared to experimental data. Except for $n = 1$ one can see an excellent agreement with the experimental data for both the energies E_n and the

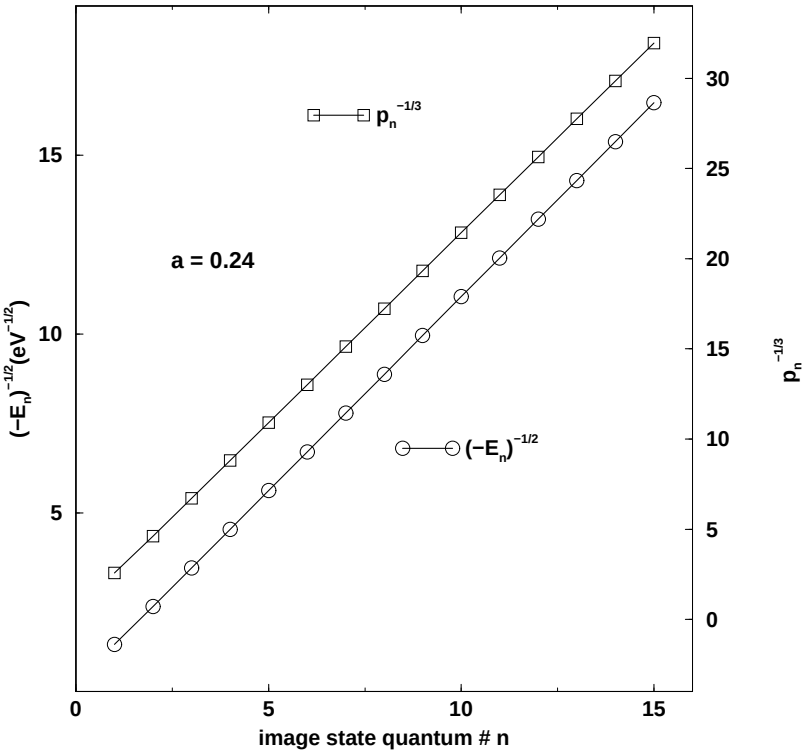

Figure 3.8: The quantities $\frac{1}{\sqrt{-E_n}}$ and $\frac{1}{\sqrt[3]{p_n}}$ for image states, plotted against the image state quantum number n. These quantities should scale proportional to n according to the approximate scaling laws (3.2) and (3.19). From this plot $A = 0.854$ eV and $a = 0.24$.

lifetimes τ_n. For example for $n = 3$ the rather simple model (3.20) gives a lifetime of 337 fs, the more elaborate calculations which are using the electron self-energy [120] give 367 fs compared with an experimental value of 300±20 in [18]. For higher image states, much longer lifetimes are obtained according to an approximate scaling law $\tau_n \propto n^3$ [75].

(III) Other eigenstates of $\hat{H}_0$ used for dynamics

The other states included in the eigenstate basis used in the dynamical calculations below are chosen as follows. Because a one electron pseudo potential is used the electron-electron interaction is already implicitly included in the

potential term. This should be no problem for the image potential and continuum states, because only a small amount of electron density is transferred into these states by the pump and probe laser pulse and one can simulate the dynamics in these state in a one electron picture. Contrary for the bulk conduction band states the electron dynamics simply cannot be simulated in a one particle fashion. But since one here is not interested in the dynamics in these states, but rather the dynamics in the image potential states, which is initiated by a transition from the conduction band states, one can simply neglect all effects arising from the electron-electron interaction between the conduction band states. To this end we carry out various dynamics calculations in which only a single, bound, occupied conduction band state is taken into account as initial state. Various propagations are carried out with a number of possible initial states in the proper energy range below the Fermi level, and the results are incoherently averaged (with equal weighting) over the initial conditions to arrive at the final results. Altogether 17 initial, occupied bulk states are taken into account with energies from -5.49 eV to E_{Fermi} = -4.62 eV. Since $\hbar(\omega_{pump} + \omega_{probe}) = 6.27$ eV, one can therefore detect kinetic energies from $6.27 - 5.49 = 0.78$ to $6.27 - 4.62 = 1.65$ eV for the photo ejected electrons. This is the range of the energy-resolved 2PPE spectra to be modeled in section 3.4.

Finally three different basis sets of different size (and hence different computational effort) are applied in the propagations below. All basis sets contain one state of gerade symmetry below the Fermi energy and the first 15 image potential states of ungerade symmetry. In the "full basis set" all continuum states of gerade symmetry (≈ 140) are used in the interesting energy range from 0.7 to 1.8 eV above E_{vac}. This splitting into gerade $\leftrightarrow$ ungerade $\leftrightarrow$ gerade eigenstates is mainly motivated by numerical reasons and has some (but reasonable) "physical" consequences on the system dynamics, which will be outlined in the next section. To reduce the numerical effort another basis set with only 29 continuum states located within the energy window that can be reached by $\hbar(\omega_{pump} + \omega_{probe})$ from the initial bound state is used. This basis

set will be denoted as "29C basis" in the following. For the calculations of the time resolved 2PPE signals for a fixed photoelectron energy sometimes only one continuum function is taken into account ("1C basis"). Test calculations show that the error introduced by these approximations is reasonably small (for further details see section 3.4.3).

(IV) Dipole matrix elements

Below, the semiclassical dipole approximation is used to couple the system to an external laser field. The Hamilton operator is then

$$\hat{H}(t) = \hat{H}_0 - \epsilon(t)\hat{\mu} \tag{3.21}$$

where $\hat{\mu} = ze$ is the dipole operator of the electron. In the energy representation, one needs the dipole matrix elements

$$\mu_{ij} = \langle \psi_i(z) \mid e\ z \mid \psi_j(z) \rangle \qquad . \tag{3.22}$$

For the chosen basis sets and the symmetry of the system μ_{ij} is only non zero for transitions from the initial bulk state into an image potential state and from an image potential state into a continuum state ($g \rightarrow u$ or $u \rightarrow g$ transitions). So in our approach transitions between different image potential states and different continuum states are neglected. This is a reasonable assumption since these transitions are far off resonance for those laser frequencies used.

The dipole transition matrix elements connecting a "typical" occupied bound state ψ_B of gerade symmetry below the Fermi energy ($E_B = -4.713$ eV), to the first 15 image potential states ψ_n (of ungerade symmetry) are shown in Fig. 3.9 (solid line). Also given are transition elements connecting the (ungerade) image potential states with a "typical" unbound continuum state ψ_C of gerade symmetry ($E_C = 1.552$ eV) (dashed line). We note that the B $\rightarrow$ image states transition matrix elements are particularly large for low n, *i.e.*, a bulk electron excited by the pump laser has a good chance to end up in one of the lowest image states which are located close to the

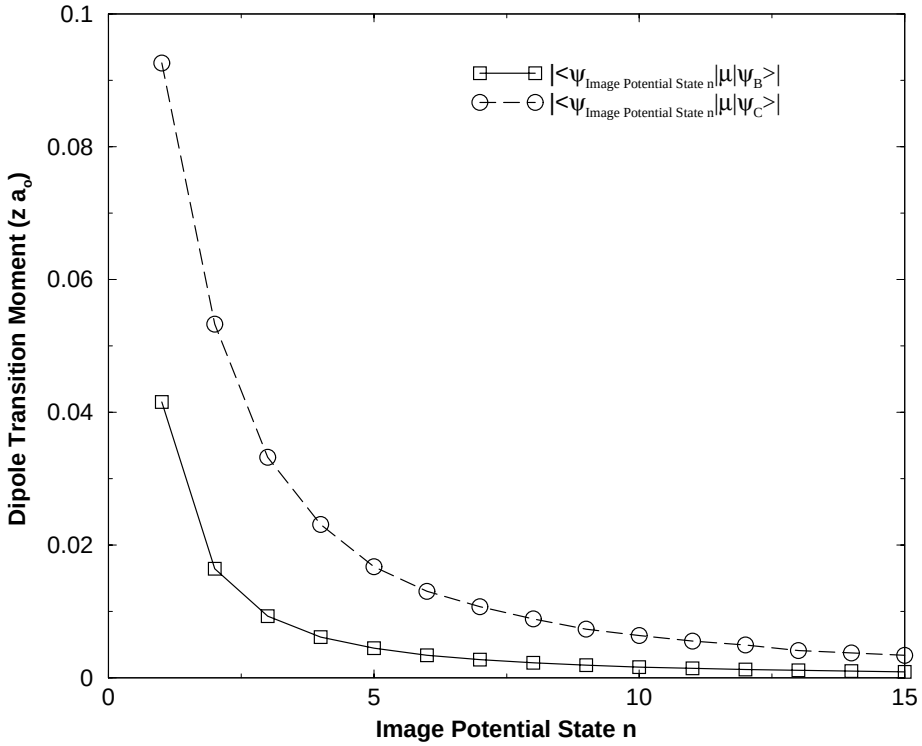

Figure 3.9: Dipole matrix elements connecting a "typical" bound, bulk state ψ_B (gerade) below the Fermi energy ($E_B = -4.713$ eV), to the first 15 image potential states ψ_n (ungerade) (solid line). The same for a "typical" unbound continuum state ψ_C ($E_C = 1.552$ eV) of gerade symmetry (dashed line).

surface. Similarly, the creation of a photo ejected electron (image states $\rightarrow$ C) by absorption of a probe photon is most likely for the lowest n. Therefore, only electrons located close to the surface can be excited with high probability thus reflecting the fact for high-n states the electron is almost "free" and does not absorb a photon. This causes characteristic quantum beats in the time resolved 2PPE spectra as will be shown below. Despite the dipole matrix elements decay quite rapidly with n, the simple $\propto n^{-3}$ scaling anticipated in Ref. [17] is not really compatible with the actual numerical results.

3.3 Propagation methods

For the simulation of 2PPE spectra 3 different, time-dependent quantum dynamical models of increasing complexity have been employed. The time-dependent approach is appropriate for the pump probe experiments at hand, and the fully quantum mechanical treatment is necessary since the dynamics of electrons is of interest. The three different models are:

1. In the "QM model" the Schrödinger equation for the system is solved. This is an ideal model in which dissipation is neglected.

2. In the "ER model" the open quantum system Liouville-von Neumann equation is solved with energy relaxation (finite lifetime of image states) included. Also dephasing effects are included, but only those associated with energy relaxation.

3. In the "FD model" also a Liouville-von Neumann equation is solved. This time, however, not only lifetime effects (energy relaxation) but also pure dephasing (phase relaxation) is included on top of dephasing related to energy relaxation.

For all propagation schemes the 2PPE signal is calculated from the populations of the continuum states after the end of the second pulse. These populations are then averaged over all initial bulk states used. The energies of the continuum states are the kinetic energies of the electrons, corresponding to the photoelectron energies measured in the experiments.

3.3.1 Wave packet dynamics

For the dissipation free case the (closed) system dynamics is given by the time-dependent Schrödinger equation

$$i\hbar\dot{\Psi}(t) = \hat{H}(t)\Psi(t) \tag{3.23}$$

with $\hat{H}(t) = \hat{H}_0 - \epsilon(t)\hat{\mu}$, where $\hat{\mu}$ is the dipole operator introduced above and $\epsilon(t)$ the external electric field of the pump and probe laser pulses, respectively.

$\epsilon(t)$ is chosen here as

$$\epsilon(t) = \epsilon_{o,pump}(t)\ \cos(\omega_{pump}t) + \epsilon_{o,probe}(t)\cos(\omega_{probe}t) \quad , \tag{3.24}$$

where the pulse envelopes are chosen as $\cos^2$ functions:

$$\epsilon_{o,i}(t) = \epsilon_{max,i}\cos^2\left[\frac{\pi}{2\sigma_i}(t - t_{p,i})\right] \quad . \tag{3.25}$$

Here, $\epsilon_{max,i}$ is the maximum field strength for pulse i (= pump or probe), σ_i is the pulse width, and $t_{p,pump}$ and $t_{p,probe}$ the times by which pump and probe pulses are maximal. The delay time between both pulses is $\Delta\tau = t_{p,pump} - t_{p,probe}$. Finally, ω_{pump} is the frequency of the pump pulse chosen as $\hbar\omega_{pump} = 4.7$ eV and $\hbar\omega_{probe} = 1.57$ eV for the probe pulse, in accordance with the experiments [17]. The widths of the pulses were also chosen as the experimental ones, *i.e.*, $\sigma_{pump} = 95$ fs and $\sigma_{probe} = 70$ fs. The maximal field strengths were chosen $\epsilon_{max,i} = 0.001\ \frac{E_h}{ea_0}$ for both pulses. Test calculations showed that the shape of the 2PPE spectra is nearly independent on the choice of $\epsilon_{max,i}$ (if chosen from reasonable ranges), even when $\epsilon_{max,pump}$ and $\epsilon_{max,probe}$ are different. Also, replacing the $\cos^2$ pulses by Gaussians has only minor effects.

The Schrödinger equation is solved using (another) split operator technique [121] during the period when either pump or probe or both pulses are "on". Accordingly, the wave packet at time $t + \Delta t$ derives from the wave packet at time t as:

$$\mid \Psi(t+\Delta t)\rangle = (e^{-i\hat{H}_0\Delta t/(2\hbar)} \cdot \mathbf{U}^\dagger e^{-i\epsilon(t)\tilde{\mu}\Delta t/\hbar}\mathbf{U} \cdot e^{-i\hat{H}_0\Delta t/(2\hbar)}) \mid \Psi(t)\rangle \quad . \tag{3.26}$$

Here, $\tilde{\mu}$ is the diagonal dipole operator in its eigenfunction space and $\mathbf{U}$ the transformation matrix from the eigenfunctions of $\hat{H}_0$ to those of $\hat{\mu}$. The time step chosen is $\Delta t = 0.097$ fs. In the absence of an external field (*i.e.*, when the delay time $\Delta\tau$ between the pulses is so large that they don't overlap), the wave function can be propagated in a single step since $\hat{H}_0$ is diagonal in the field-free eigenstate basis:

$$\begin{aligned} \mid \Psi(t_2)\rangle =& e^{-i\hat{H}_0(t_2-t_1)/\hbar} \mid \Psi(t_1)\rangle \\ =& \sum_n e^{-iE_n(t_2-t_1)/\hbar} c_n(t_1) \mid \psi_n\rangle\langle\psi_n \mid \Psi(t_1)\rangle \quad . \end{aligned} \tag{3.27}$$

Here t_1 is the time where the first laser pulse stops and t_2 where the second one starts, and E_n and ψ_n are the eigenenergies and eigenfunctions of $\hat{H}_0$, and the $c_n(t_1)$ are the expansion coefficients at the end of pump pulse.

The initial condition used in (3.23) is

$$\Psi(0) = \psi_B \quad , \tag{3.28}$$

where ψ_B is one of the (17) selected bound bulk states below the Fermi level.

3.3.2 Open system density matrix theory

The Liouville-von Neumann equation for an open quantum system [15, 122] is used to model the dissipation arising from the interaction between the electron located in the image potential with the bulk electrons:

$$\frac{\partial}{\partial t}\hat{\rho} = -\frac{i}{\hbar}\left[\hat{\hat{H}}, \hat{\rho}\right] + \dot{\hat{\rho}}_D \quad . \tag{3.29}$$

Here, the first term on the right hand side determines the change of the density operator $\hat{\rho}$ due to the Hamiltonian evolution, including electron-field coupling. For not too strong system-bath coupling $\hat{\hat{H}}$ can be taken as the system Hamiltonian $\hat{H}(t)$. The second term on the right hand side describes the coupling of the "system" (the active electron), to the "bath" (of inactive bulk electrons). This term accounts for energy relaxation and energy relaxation related phase relaxation, as well as for pure dephasing (see below). The Liouville-von Neumann equation is solved within the Lindblad dynamical semigroup approach [123, 124] which includes the Markov approximation for the dissipative part. If the field-free system eigenstate basis is used, the equations of motion for the diagonal and the off-diagonal elements of the density matrix become

$$\frac{\partial \rho_{nn}}{\partial t} = \sum_{p}^{N} \underbrace{[-\frac{i}{\hbar}\left[V_{np}(t)\rho_{pn} - \rho_{np}V_{pn}(t)\right]}_{\text{system-field coupling}} + \underbrace{(W_{np}\rho_{pp} - W_{pn}\rho_{nn})]}_{\text{energy relaxation}} \tag{3.30}$$

and

$$\frac{\partial \rho_{mn}}{\partial t} = -\frac{i}{\hbar}\left[\left(E_m - E_n\right)\rho_{mn} + \sum_p^N \left[V_{mp}(t)\rho_{pn} - \rho_{mp}V_{pn}(t)\right]\right] - \gamma_{mn}\rho_{mn} \ , \tag{3.31}$$

respectively. The diagonal element ρ_{nn} is interpreted in density matrix theory as the population of state n. The off diagonal elements ρ_{mn} are the so called coherences which determine, for example, the linewidths in spectroscopy. The diagonal elements are influenced by the coupling of the system to the field, and to the bath. Hence, one source of population transfer between states is due to the field-coupling terms $V_{mn}(t)$ in Eq. (3.24):

$$V_{mn}(t) = -\mu_{nm}\epsilon(t) \quad . \tag{3.32}$$

The electron-field coupling leads also to the build up of coherences [Eq. (3.31)].

The coupling of the active electron to the "bath" leads also to population transfer, modeled by the energy relaxation rates W_{mn}

$$W_{mn} = \frac{1}{T_{1_{m,n}}} \quad . \tag{3.33}$$

The characteristic timescale for population (energy) transfer is $T_{1_{m,n}}$. Further, coherences can decay by dephasing effects. These are described by a dephasing rate γ_{mn} in (3.31), which has two contributions:

$$\gamma_{mn} = \frac{1}{2T_{1_{m,n}}} + \frac{1}{T^*_{2_{m,n}}} \ . \tag{3.34}$$

The first term on the right hand side is related to the energy relaxation time $T_{1_{m,n}}$, while the second one accounts for pure dephasing on a timescale $T^*_{2_{m,n}}$. The finite time $T_{1_{m,n}}$ is microscopically motivated by *inelastic* interaction of the system (active electron) with the bath (the bulk electrons). The pure dephasing time $T^*_{2_{m,n}}$ leads to a loss of coherence but no population transfer between states m and n, and is due to *elastic* interaction between the system and the bath. Experimentally [18] is was found that the pure dephasing

rates can be "controlled" if the Cu surface is covered with CO adsorbates; a higher coverage with CO leads to much faster dephasing. Here we will restrict ourselves to the clean Cu(100) surface for which, however, still some amount of pure dephasing is present [18].

The T_1 and T_2^* times are chosen as follows. A bath temperature of zero Kelvin is used and therefore all rates for upward transitions induced by the bath are identical to zero and so the corresponding T_1 times are ∞. Further it is assumed that dissipation acts only on the image potential states and has no effect on the continuum states. Finally the T_1 relaxations are assumed to transfer population only from the image potential states into the bound state ψ_B below E_{Fermi} which was selected as an initial state and from where the electron is excited by the pump pulse. Dissipative transitions between the image potential states are neglected. This means that Eq. (3.33) is approximated as

$$W_{mn} = \begin{cases} \delta_{mB}\frac{1}{\tau_n}, \text{if } n = \text{ image state} \\ 0 \qquad , \text{else} \end{cases} \tag{3.35}$$

and τ_n is the (inelastic) lifetime of image state n. For the latter we take the experimental lifetime of $\tau_1 = 40$ fs for image state $n = 1$ [18], but the calculated lifetimes τ_n according to the penetration formula (3.20) for all higher n. The calculated lifetimes of the lower image states up to $n = 6$ have been given already in Table 3.3 - a complete list up to $n = 15$ is provided in Table 3.4. As mentioned earlier, there are more elaborate theoretical calculations of image potential state lifetimes (for an overview see Ref. [78]), but since the simple model given in Eq. (3.3) is known to be fairly accurate for image potential states with $n \geq 2$, here these lifetimes are used. It should also be noted that the more sophisticated theoretical models rarely have been applied to image states with $n > 3$.

However, one must assume that in reality most of the relaxation is not into the initial bulk state alone but into unoccupied states above the Fermi energy as suggested in Eq. (3.35). In other words the lifetime of image state

n,

$$\frac{1}{\tau_n} = \sum_{m \neq n} \frac{1}{T_{1_{m,n}}} \quad , \tag{3.36}$$

has in reality contributions from all (empty) final states $m \neq n$ below n. To estimate the error introduced by the simplification (3.35) a test calculation was made where the image potential states were allowed to decay also in other bulk continuum states (with zero dipole transition matrix elements). The difference between these two approaches turned out to be very small so that the final state resolution of dissipation appears to be unimportant.

The pure dephasing processes are again assumed to act only on coherences between two image potential states m and n . The pure dephasing rates are parameterized as

$$\frac{1}{T^*_{2_{m,n}}} = \frac{c}{4}\left(\frac{1}{\tau_m} + \frac{1}{\tau_n}\right) \quad . \tag{3.37}$$

Three different values for c are used, namely 0.5 ("weak" pure dephasing), 1.0 ("normal" pure dephasing) and 2.0 ("strong" pure dephasing). The experimental data [18] suggest that the normal dephasing model should be the most appropriate for the clean Cu(100) surface. Unfortunately, the experimentally measured T_2^* values have a very large uncertainty. Several selected T_2^* times for "normal" pure dephasing are given in Table 3.4.

A matrix propagator based on a Newton polynomial of 16-th order is used to solve the Liouville-von Neumann equation (for further details see Refs. [125] and [126]). The time step chosen is 0.048 fs.

n	τ_n/[fs]	$T^*_{2_{n,n+1}}$/[fs]	$T^*_{2_{n,n+2}}$/[fs]	$T^*_{2_{n,n+3}}$/[fs]	$T^*_{2_{n,n+4}}$/[fs]
1	40	117.989	143.01	151.958	155.649
2	112.342	336.94	391.218	416.656	429.458
3	336.686	931.709	1090.23	1182.46	1236.97
4	755.824	1978.34	2304.52	2521.07	2664.02
5	1430.96	3598.75	4156.25	4559.63	4847.51
6	2423.29	5915.12	6767.12	7421.22	7915.3
7	3794.04	9049.73	10258.9	11227.8	11991.4
8	5604.41	13124.9	14753.7	16101	17198.1
9	7915.62	18263.1	20373.4	22162.5	23657.4
10	10788.9	24586.7	27240.4	29534.3	31490.8
11	14285.4	32218	35476.9	38338.2	40820.2
12	18466.3	41279.5	45205.1	48696.4	-
13	23393	51893.7	56547.7	-	-
14	29126.5	64182.8	-	-	-
15	35728.3	-	-	-	-

Table 3.4: Lifetimes τ_n and several pure dephasing times T_2^* used in the density matrix FD and ER models. These times are evaluated using Eqs. (3.20) (except for τ_1), and (3.37) with a "normal" pure dephasing strength ($c = 1$).

3.4 Results and discussion

In the following the calculated 2PPE spectra for the different models given in the previous section will be compared with each other and with experimental data from [17, 18] and [16]. All the experimental curves shown in this section were measured in the group of Prof. U. Höfer (Marburg), who kindly made these data available. First in section 3.4.1 energy resolved spectra for different delay times will be examined. Then in section 3.4.2 time resolved cuts through these spectra for fixed photo electron energies will be used to gain more detailed insight into the coherent system dynamics.

3.4.1 Energy resolved spectra

Fig. 3.10(b) shows the experimental energy resolved 2PPE signals at zero delay time $\Delta\tau$ between pump and probe pulse in comparison to theoretical results obtained in the full dissipation (FD) model with "normal" pure dephasing. In Fig. 3.10(a) the FD model data is compared to the QM model, where no dissipation was included. For all cases one can see three peaks centered around $E_{kin} = 1.0$ eV, 1.4 eV and 1.5 eV. The first two peaks correspond to electrons photo ejected from image states $n = 1$ and 2. The third peak comes from the image states with $n > 2$, for which the level spacing is already so small that they cannot be individually resolved energetically. The assignment is based on energy conservation for the photo ionization step, *i.e.*,

$$\hbar\omega_{probe} + E_n = E_{kin}(n) \quad , \tag{3.38}$$

where $E_{kin}(n)$ is the kinetic energy of the electron photo ejected from image potential state n with energy E_n. With $\hbar\omega_{probe} = 1.57$ eV and $E_1 \approx -0.56$ eV, $E_2 \approx -0.17$ eV, $E_3 \approx -0.07$ eV (see Table 3.3 with $\mathrm{E}_{Fermi} = -4.62$ eV), we get $E_{kin}(1) \approx 1.01$ eV, $E_{kin}(2) \approx 1.4$ eV, $E_{kin}(n > 2) \geq 1.5$ eV.

Let us first compare the experimental spectrum with the results from the FD model ("normal" pure dephasing) [Fig. 3.10(b)]. One can see that the FD model reproduces the experimental peak position and width nearly

perfectly for the $n = 1$ image potential state. In both spectra the linewidth [Full Width at Half Maximum (FWHM)] of the $n = 1$ peak is $\Gamma_1 \approx 70$ meV. For the higher image potential states the agreement concerning the position and width is still very good. Both theory and experiment only resolve the first two peaks clearly. There is some quantitative deviation between theory and experiment with respect to peak intensities. For example, the ratio of intensities of the $n = 1$ to the higher-n peaks is too small in theory, making the $n \geq 2$ peaks relatively more pronounced than in experiment. This may be due to the possibility that the $n = 1$ image state wave function is not accurately enough represented by the model, and hence the transition dipole moments to and from this states are not, either. (Recall that the lifetime τ_1 when calculated based on the penetration argument was clearly too low.) Despite these deviations in detail, the overall trends also in the intensities are correct.

If we now compare the theoretical data from the QM model with the FD model spectrum [Fig. 3.10(a)], one can see, that for zero delay time $\Delta\tau$ dissipation only affects the intensity of the first two peaks, corresponding to those image potential states with the shortest lifetimes. One also notes that the linewidth is mainly determined by the laser pulse and not by the finite lifetime (intrinsic linewidth) of the image potential state. For $n = 1$ one gets a width of $\Gamma_1 \approx 60$ meV for the "dissipation free" QM model, which is only ≈ 10 meV narrower than for the FD model. Therefore, here it is not possible to determine the lifetime from the linewidth and *vice versa*. The relationship between intrinsic linewidth Γ and the lifetime τ is

$$\Gamma \, \tau \geq \hbar \quad . \tag{3.39}$$

For $n = 1$ this results in an intrinsic linewidth of $\Gamma_1 \geq 16$ meV for a lifetime of $\tau_1 = 40$ fs. The ">" accounts for additional broadening due to pure dephasing effects, which are expected to be not that important, however, for clean Cu(100).

More accurate information about the lifetimes of the first three image potential states can be obtained by recording several energy resolved 2PPE

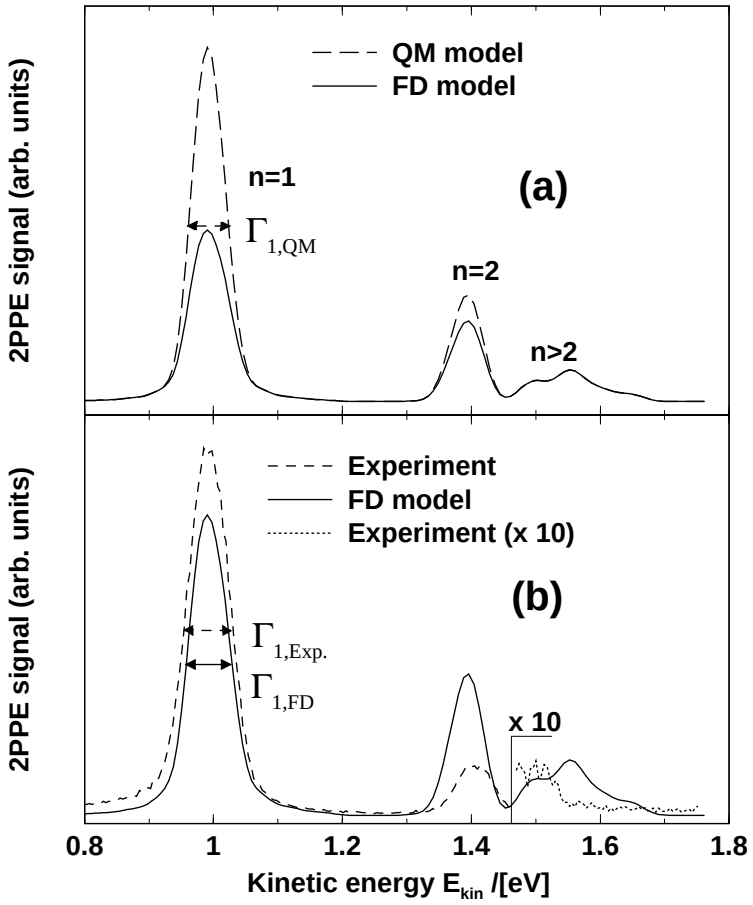

Figure 3.10: (a) Calculated 2PPE signal at zero delay time $\Delta\tau$ for the full dissipation (FD) model with "normal" pure dephasing, and the dissipation free QM model (29C basis set). (b) Comparison between the experimental 2PPE [17] signal with the FD data. The region above $E_{kin} = 1.46$ eV is scaled by the factor of ten in intensity for the experimental spectrum. The linewidths Γ_1 (FWHM) for $n = 1$ are indicated by arrows in (a) for the QM model, and in (b) for the FD model and experimental data, respectively.

spectra for different delay times $\Delta\tau$. These spectra are given in Fig. 3.11 (a) (theoretical data for the FD model with "normal" pure dephasing), and Fig. 3.11 (b) (experimental data). The upper part of the graphs shows spectra for delay times from -70 fs to +200 fs, the second spectrum in each graph being the one for zero delay time, which was already shown in Fig. 3.10(b). Delay times of up to 800 fs are considered in the lower part of 3.11. One can see that after $\Delta\tau = 200$ fs the peak for $n = 1$ has nearly vanished both in theory and experiment. This is because the $n = 1$ population has already almost completely decayed into the bulk by the time the probe pulse arrives (recall that $\tau_1 = 40$ fs.) After $\Delta\tau = 800$ fs, also the peaks for $n = 2$ and 3 are virtually unvisible (the large remaining peak in the theoretical spectra corresponds to states with $n > 3$), because $\tau_2 = 112$ and $\tau_3 = 337$ fs according to Table 3.4. Through a careful examination of peak intensities for different delay times one can therefore determine the lifetimes for the first three image potential states. Unfortunately, due to the large spectral width of the laser pulses – and in the experimental case noise and low signal intensity – no accurate information can be extracted for the image potential states $n > 3$ from the energy resolved spectra.

3.4.2 Time resolved spectra

In the time domain much more information about the image potential states can be obtained. Due to the considerable bandwidth of the pump pulse (remember here in all cases $\sigma_{pump} = 95$ fs and $\sigma_{probe} = 70$ fs) a coherent superposition of higher image potential states ($n > 2$) is excited. The lower limit for the energetic width of the pump pulse is $\Delta E \geq \frac{\hbar}{\sigma_{pump}} = 7$ meV. This means that for $n = 1$ and $n = 2$ with a level spacing of $\Delta E_{2,1} = E_2 - E_1 = 397$ meV (see Table 3.3) the finite bandwidth of the pump pulse has no effect. However, $E_{4,3} = 35$ meV, $\Delta E_{6,5} = 10$ meV, and $\Delta E_{8,7} = 4$ meV, demonstrating that the higher-n states are never excited "alone".

For simplicity let us first examine the results for the QM model, where no effects of dissipation have been included. Fig. 3.12 shows a contour plot

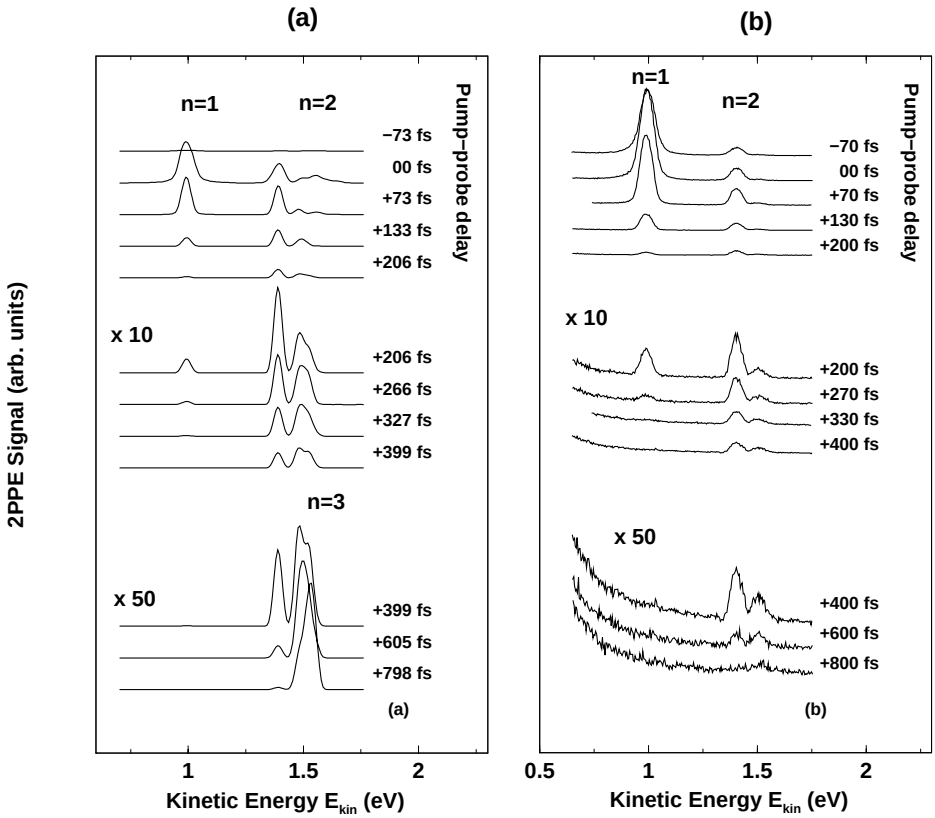

Figure 3.11: (a) Calculated energy resolved 2PPE signals for different delay times $\Delta\tau$ between pump and probe pulse, for the FD model with "normal" pure dephasing (29C basis set). The small numbers on the left indicate the pump probe delay time. The first five spectra at the top of the graph have the same intensity scale. For the others the scale is given by the large numbers at the left. (b) The corresponding experimental 2PPE signals [16].

of the calculated energy and time resolved 2PPE signal for delay times from $\Delta\tau$ =-0.2 ps to $\Delta\tau$ = 1.5 ps for the dissipation free QM model. In this two dimensional spectrum the photo electron signal is a function of the two key parameters, namely the pump probe delay time and the electron kinetic energy. So a one dimensional cut for a fixed delay time along the kinetic energy axis gives an energy resolved 2PPE spectrum like the ones shown in section 3.4, while a one dimensional cut for a fixed kinetic energy along the delay time axis results in a TR-2PPE spectrum.

In Fig. 3.12 one can see an almost constant signal as a function of $\Delta\tau$ for the image potential states $n = 1$ and 2 after the pulses are completely separated. The peak for higher image potential states around above $E_{kin} =$ 1.5 eV shows a distinct quantum beat pattern caused by coherences between these states. This can be explained by a coherent motion of an electron wave packet created by the pump pulse. The motion of this wave packet will be discussed below. In a simple classical picture one can say the electron moves back and forth in front of the surface. Then it can only be efficiently transferred into continuum states when located near the surface, because far away from the surface the electron is almost a free electron and therefore does not adsorb a photon [see section 3.2(IV)]. Therefore, the TR-2PPE signal shows the proximity of the moving electron to the surface and the oscillation period of its motion. As one can already see from Fig. 3.12, there is not only a single frequency but many different ones, depending on E_{kin}. This is because in the appropriate quantum mechanical picture there are coherences between many image potential states and each coherence contributes with its own beating frequency $\nu_{ij} = (E_j - E_i)/h$ to the spectrum. This also explains why the isolated peak for very high energies (around $E_{kin} = 1.56$ eV) at zero delay time, shows no recurrence at longer $\Delta\tau$ on the time scale shown. This peak is mainly due to the creation of a electronic wave packet consisting of high lying image potential states ($n \geq 10$). In this energy region the level spacing is very small and therefore the oscillatory periods for coherences of neighboring states are large. For example for $n = 10$ and $n = 11$ the period

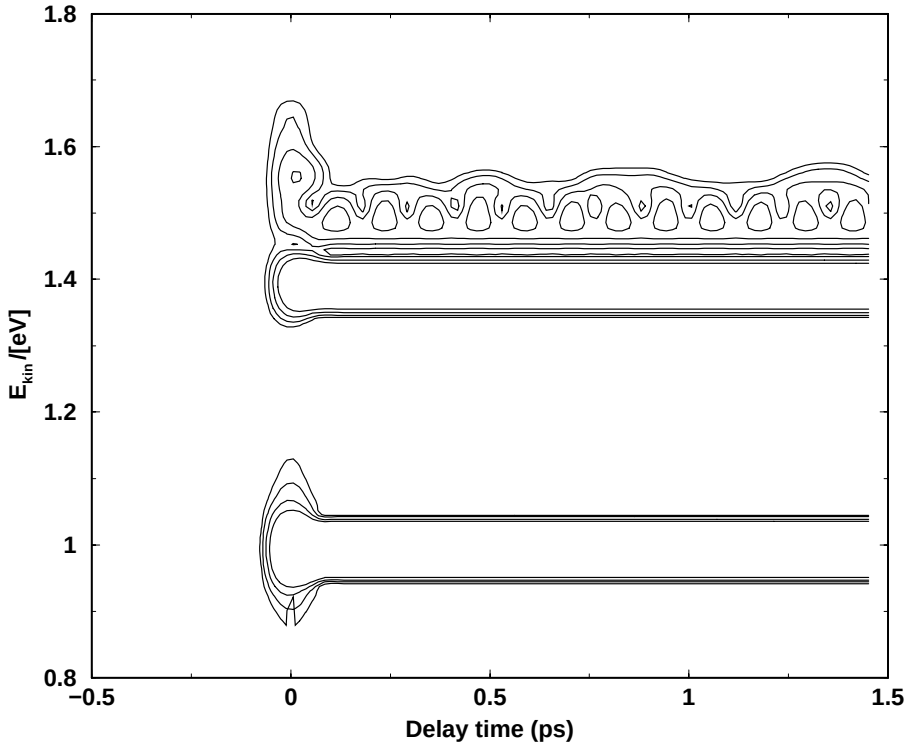

Figure 3.12: Theoretical two-dimensional 2PPE signal as a function of electron kinetic energy E_{kin} and delay time $\Delta\tau$, for the dissipation free QM model (29C basis set). The contour lines are at 1, 0.5 , 0.25, 0.125 signal intensities (arb. units), and chosen to resolve especially the quantum beat patterns for the peaks $n > 2$.

$T_{10,11} = \nu_{10,11}^{-1} = \frac{h}{E_{11}-E_{10}}$ is already 2.1 ps. If one now keeps in mind that many neighboring states contribute to the wave packet in this region, one can simply not expect recurrences on the time scale of shorter than 2 ps.

To include the effects of energy and phase relaxation, the same spectrum was calculated within the FD model. The result is shown in Fig. 3.13, as a surface plot of the 2PPE signal as a function of the kinetic energy and the pump probe delay time. The energetic region of the higher image potential states is scaled by a factor of five in the energy axis and the signal intensity. One can see the rather rapid decay of the signals for $n = 1$ and 2 around

$E_{kin} = 1.0$ and 1.4 eV, which is due to their short lifetimes. In the magnified region the quantum beat patterns for the higher image states are shown. These patterns are less pronounced than in the dissipation free case, and they get progressively weaker for longer delay times. This is clearly due to the loss of population and coherence by energy relaxation and dephasing.

The effects of dissipation on the coherent motion of the electron wave packet is also illustrated in Fig. 3.14. The picture shows the time-dependent electron density in front of the surface up to a distance of ≈ 500 Å for a single calculation in the FD model ("normal" pure dephasing). For clarity of presentation, the results for a single initial state are shown and no incoherent averaging over initial states was done. The initial bound state used has an energy of $E_B = -4.713$ eV which leads to a coherent excitation of image states centered around $n = 6$; further, no probe pulse is applied. One observes the creation of a fairly localized electron wave packet near the surface during the pump pulse. Then the wave packet begins to move outwards like one would expect. But already ≈ 0.5 ps after the maximum intensity of the pump pulse a large part of the wave packet has returned near to the surface while another one continues to move away from the surface. Afterwards the electron density delocalizes and spreads over a large area while at the same time more and more density relaxes back into the bulk. This is because population and coherence is lost in the image potential states due to the dissipation processes. The creation of an electron wave packet outside the surface by a pump pulse and the subsequent dissipative decay is further demonstrated in Fig. 3.15. In this figure the total population of all image states is shown together with a few individual state populations around $n = 6$. One recognizes the rapid build up of population following the pump pulse, and the subsequent exponential decays of the different individual image states with their characteristic, n-dependent lifetimes.

To get more precise information about the underlying dynamics 2PPE signals for a fixed photo electron energy at different delay times will be examined and compared to experimental data in the following. This corresponds

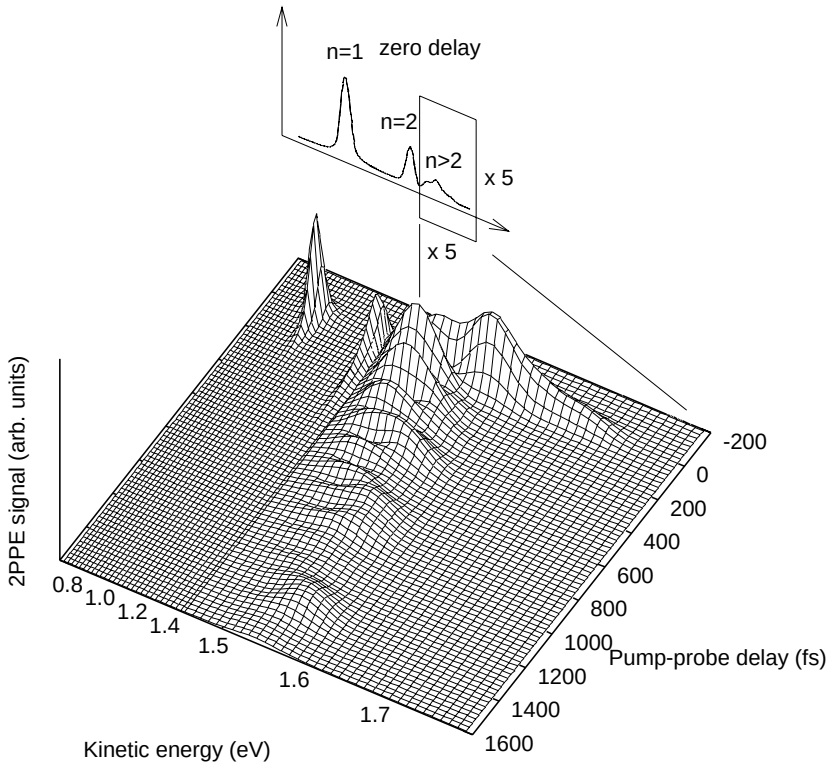

Figure 3.13: Theoretical two-dimensional 2PPE signal as a function of electron kinetic energy E_{kin} and delay time $\Delta\tau$, within the full dissipation (FD) model (29C basis set and "normal" pure dephasing). The energy region showing quantum beat patterns is magnified by a factor of five along the energy and intensity axes.

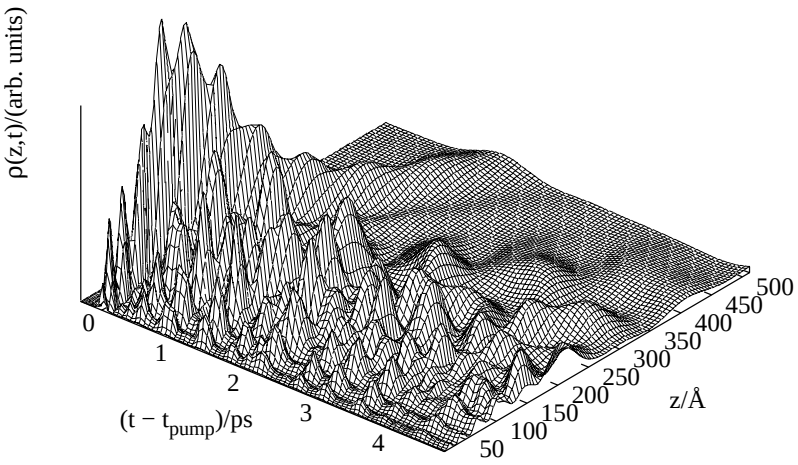

Figure 3.14: Time-dependent electron density near the surface region. The surface layer is located at $z = 0$ in this figure. Shown is the density for a transition from one initial bulk state near the Fermi energy ($E_B = -4.713.$ eV). In this case, a coherent superposition of image potential states around $n = 6$ is created. The full dissipation (FD) model with "normal" pure dephasing is used. No probe pulse is applied and t_{pump} is the time for which the pump pulse has the maximum intensity.

to carrying out one dimensional cuts along $\Delta\tau$ for a given E_{kin} in Figs. 3.12 or 3.13.

Fig. 3.16 (a) shows the calculated time-dependent 2PPE signals for a photo electron energy of $E_{kin} = 1.552$ eV for all theoretical models used. This photo electron energy corresponds to an electron wave packet with a binding energy of $E_b \approx 15$ meV in the image potential before the probe pulse. An energy of -15 meV relative to E_{vac} means that the wave packet consists of a superposition of image potential states centered around $n = 7$. An illustration of this coherent excitation is given in 3.16 (c). For $n = 7$ the level

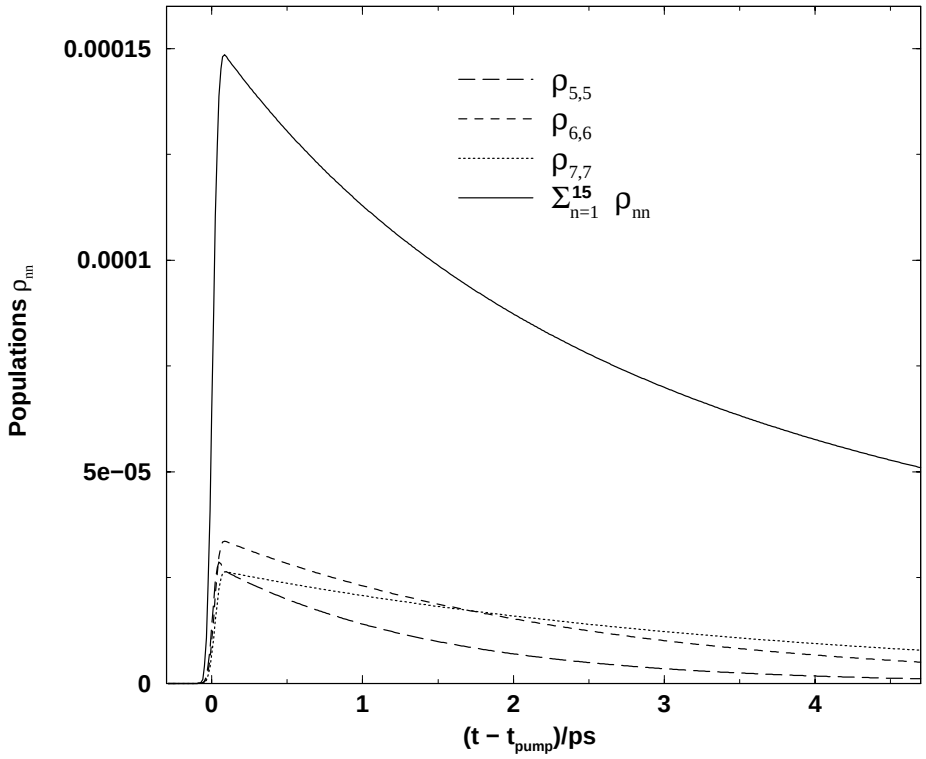

Figure 3.15: Total population of all image states together with a few individual state populations around $n = 6$ created by the pump pulse for a transition from one initial bulk state near the Fermi energy ($E_B = -4.713.$ eV). The theoretical model and propagation parameters are the same as in Fig. 3.14.

spacing is already quite small. For example, $E_8 - E_7 \approx 4$ meV (see above), and $E_7 - E_6 \approx 6$ meV. This corresponds to an oscillation period of $T_{8,7} \approx 1.1$ ps and $T_{7,6} \approx 0.7$ ps, respectively. Therefore, the calculated signal without dissipation [QM model, Fig. 3.16 (a)] shows pronounced partial recurrences for longer delay times. These recurrences are much weaker when energy relaxation is included in the ER model. In this case one can clearly see the decay caused by loss of population and coherence due to the energy relaxation process. The full dissipation model (FD) adds more loss of coherence by pure dephasing processes. This leads to a "smearing out" of the signal for longer delay times. The influence of pure dephasing can be seen in Fig. 3.16 (b) where the signals for different dephasing strengths are compared. The spectrum is less structured for strong pure dephasing (*i.e.*, small T_2^* times), which corresponds to less pronounced recurrences of the wave packet near the surface.

In Fig. 3.17 the theoretical data for the FD model is compared with the experiment, again for a binding energy of $E_b \approx 15$ meV (b) and additionally for a binding energy of $E_b \approx 40$ meV (a). At $E_b = 40$ meV a coherent superposition of image potential states mainly with n =4, 5, and 6 is created. The corresponding kinetic energy of the photo electrons is 1.527 eV. The level spacing is larger here and so the oscillation periods much shorter ($T_{5,4} \approx 250$ fs , $T_{6,5} \approx 440$ fs). It is clearly seen that for both energies the agreement between theory and experiment is very good. Again the intensities are not so well reproduced, but for nearly every peak in the experimental spectra a corresponding peak or at least a shoulder at almost or exactly the same position can be found in the theoretical spectra. So one can say that with the FD model the system dynamics can be simulated with a very high level of accuracy.

If one looks again at Fig. 3.16 and the rather small difference between the FD and ER model, the question arises how important the pure dephasing processes really are with respect to the system dynamics. In Ref. [18] strong experimental evidence is given for these dephasing processes but it is rather

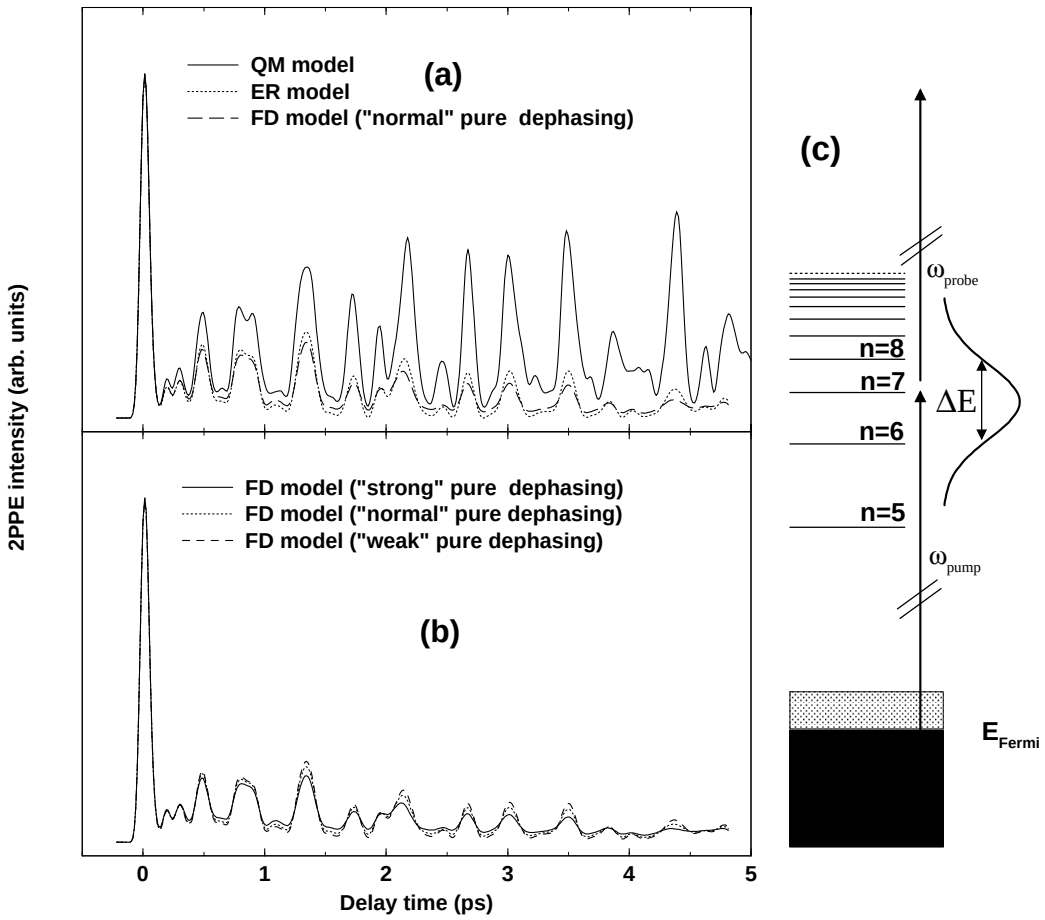

Figure 3.16: Calculated 2PPE signal for a binding energy of E_b =15 meV (E_{kin} = 1.552 eV), for all theoretical models used (1C basis set). (a) shows the spectra for the QM, ER and FD ("normal" pure dephasing) models. (b) gives a comparison between the different pure dephasing strengths used within the FD model. (c) shows a sketch of the coherent excitation of image states due to the finite width ΔE of the pump pulse.

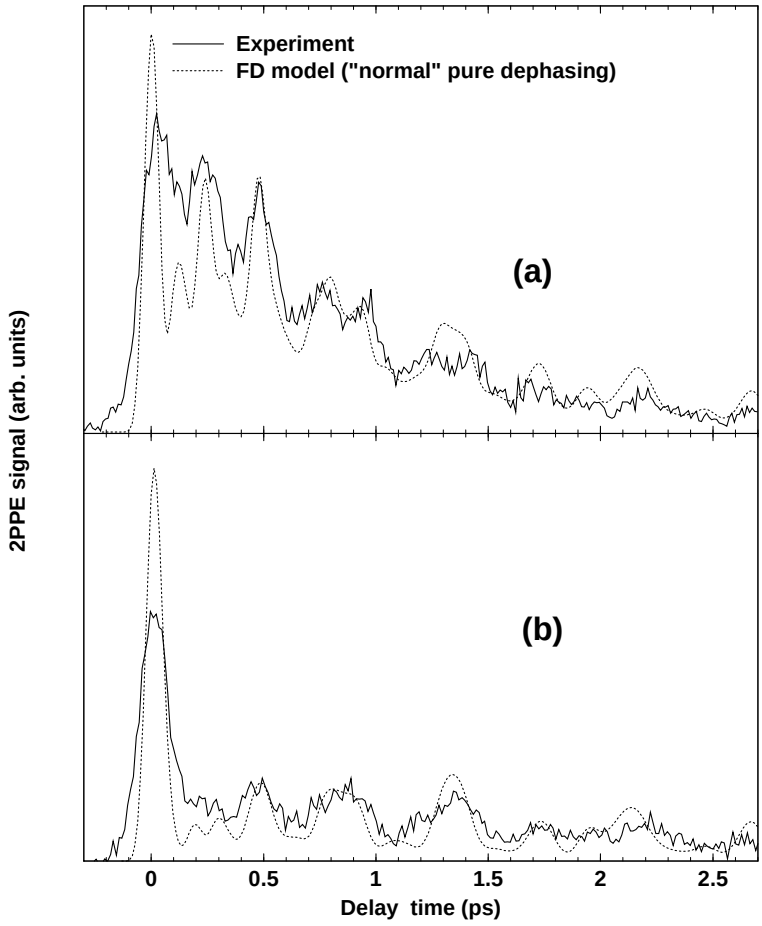

Figure 3.17: Calculated 2PPE signals for binding energies of $E_b = 40$ meV ($E_{kin} = 1.527$ eV) (a), and E_b =15 meV ($E_{kin} = 1.552$ eV) (b), for the FD model with "normal" pure dephasing (1C basis set), shown as dotted lines. The corresponding experimental data is given by solid lines.

difficult to extract the pure dephasing rates from the spectra and the obtained values have a large uncertainty. Here a closer look at the TR-2PPE spectrum for $E_b = 40$ meV is taken to investigate the role of pure dephasing. In Fig. 3.18 on the left this spectrum is shown as a solid line for (a) the experiment, (b) the ER model and (c) the FD model. From all these spectra the signal for positive delay times is taken and an exponential decay function ($\sim e^{-\Delta\tau/\tau}$, with $\tau = 0.91$ ps^{-1}) is subtracted, to roughly account for the signal decay by population transfer to the bulk. The exponential is shown as a thick dashed line and the remaining signals as thin dotted lines. The "energy relaxation corrected" signals are then Fourier transformed to the frequency domain. The obtained data points of the Fourier transforms are given as circles on the right hand side of Fig. 3.18. One can see in all spectra three main frequency components in the range from 2 to 7 THz, namely those for the superposition of $n = 5, 6$, $n = 4, 5$, and $n = 4, 6$, respectively. The overall agreement of the theoretical data with the experiment with respect to frequencies and intensities [17] is again very good. If one has a closer look at the Fourier transforms for the FD (c) and ER (b) models, one can notice only one real difference. The large peak around 4 THz has a little shoulder on the right side for the FD model, whereas in the ER model at this a position a small separate peak can be seen. In the experiment, also only a shoulder is found at this frequency [17]. This is certainly not a proof but perhaps an indication that the FD model gives a more accurate description of the dynamics than the ER model, since one knows from the experiment that pure dephasing processes are present. However, even if the pure dephasing seems to be of minor importance here, it is known experimentally [18] that for example in the case of a CO covered Cu surface pure dephasing processes become more pronounced and cannot be neglected.

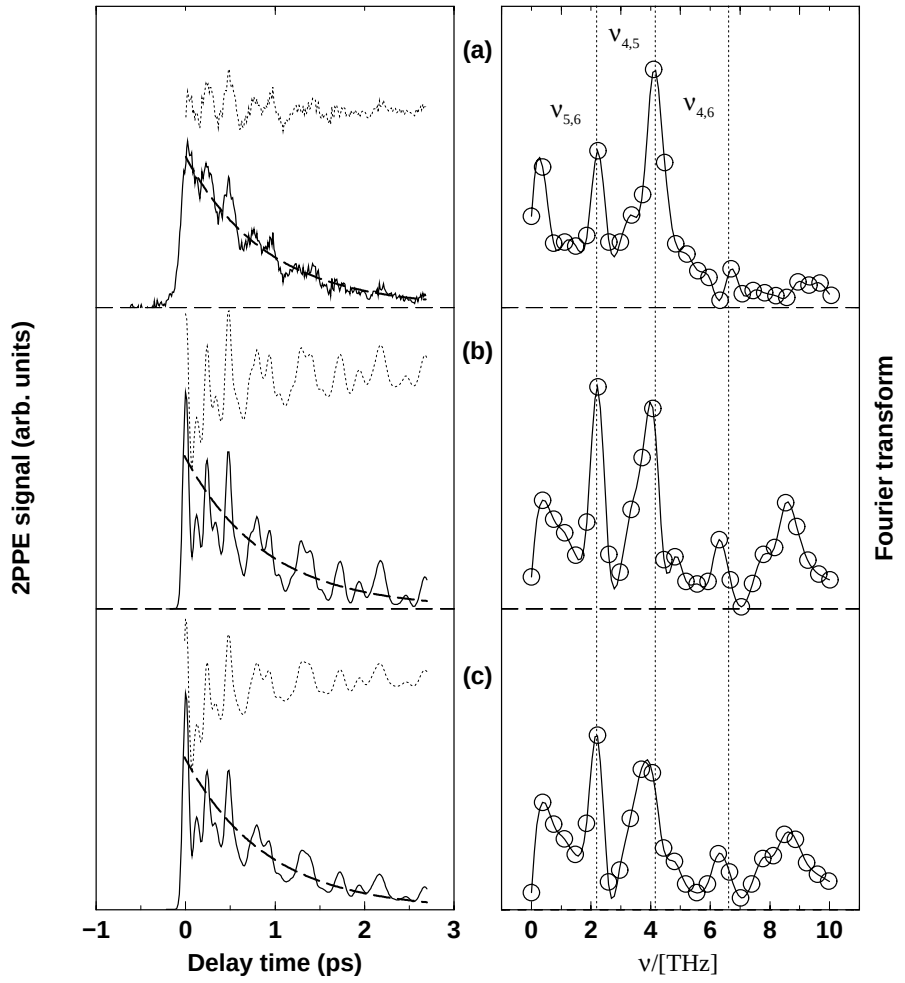

Figure 3.18: The TR-2PPE signals at a binding energy around $E_b = 40$meV (solid lines in the left graph) for (a) experimental data, (b) ER model and (c) FD model ("normal" pure dephasing). The Fourier transforms (circles in the right graph) are obtained from the signal for positive delay times after subtracting the same exponential function (thick dashed line) from all spectra. The solid lines on the right are cubic spline interpolations between the raw data. The thin dotted lines above the original signal are the curves used for the Fourier transformation. Indicated by vertical dotted lines on the right are beating frequencies $\nu_{m,n}$ between some image potential states.

3.4.3 Comparison between different basis sets

As already outlined in section 3.2 different basis sets were used in the propagations presented here, namely the 29C and 1C basis set. These were compared to the benchmark "full basis set", which contains all discretized continuum functions in the relevant energy region. The full basis set contains about 140 continuum functions, the 29C basis set 29 and the 1C basis set one, respectively. To estimate the error introduced by the reduction of basis set size, an energy resolved 2PPE spectrum for zero delay time was calculated for the full basis set and the 29C basis set in the QM model. Further, time resolved spectra for $E_b = 40$ meV were calculated with the 29C and 1C basis set with the QM and ER model, respectively. The results are shown in Fig. 3.19. Fig. 3.19 (a) gives a comparison between the full basis and the 29C basis set and (b) a comparison between the 29C basis and the 1C basis set. One can see that the error is reasonably small ($< 1\%$). The reduction of the basis set size is very important for numerical feasibility, keeping in mind that the computational effort scales as the square of the number of basis function for the QM model and as the cube for the ER and FD model.

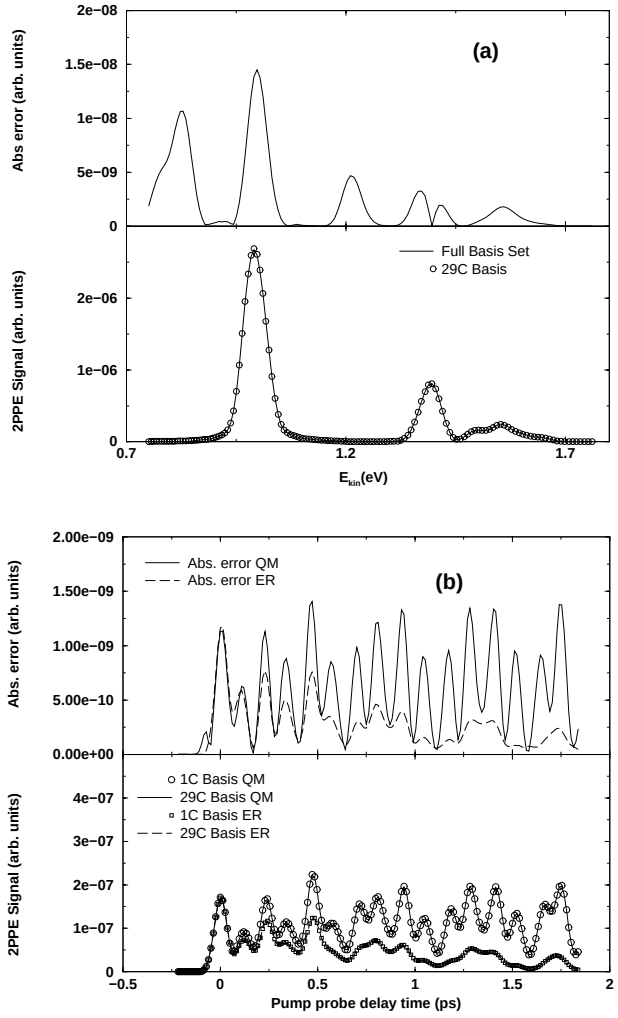

Figure 3.19: Comparison of results for different basis sets. (a) shows the energy resolved 2PPE spectra at zero delay time $\Delta\tau$ (lower graph) in the QM model for the full basis set (solid line) and the 29C basis set (circles). Shown above is the absolute difference between both spectra. (b) shows time resolved 2PPE spectra at $E_b = 40$ meV (lower graph) for [i] QM model 29C basis (solid line), [ii] QM model 1C basis (circles), [iii] ER model 29C basis (dashed line) and [iv] ER model 1C basis (squares). Above is shown the absolute error for the QM model calculations (solid line) and the ER model calculations (dashed line).

3.5 Summary and conclusions

The energies and electronic eigenfunctions of image potential states on a Cu(100) surface up to $n = 15$ were calculated using a one electron potential from Chulkov *et.al.* [89]. High accuracy was achieved by adopting the mapped Fourier grid Hamiltonian method [110] for a 601 layer Cu slab. For the same system the upper conduction band states, and a discretized set of continuum states were determined. In an eigenstate basis derived from these states dynamical simulations were performed to simulate recent energy and time resolved femtosecond two-photon-photoemission experiments. The system dynamics were calculated by means of the time-dependent Schrödinger equation (no dissipation effects) and the open quantum system Liouville-von Neumann equation (phenomenological system bath coupling to model the interactions between image potential states and conduction band states). The relaxation and dephasing rates entering the density matrix calculations were determined using a simple but in this case rather successful model which uses the bulk penetration of an image potential state.

The density matrix calculations agreed with experimental data almost quantitatively in energies, lifetimes, signal positions and widths (for energy resolved 2PPE), and quantum beat locations (TR-2PPE spectra). Minor differences between theory and experiment where found for peak intensities. That indicates that the system dynamics can be modeled in a highly accurate fashion within the theoretical model presented in this thesis. Also some theoretical indication for the importance of pure dephasing processes could be given.

Very clearly the importance of non rigidity of the surface could be demonstrated. With the "rigid surface model" (*i.e.*, the QM model) it was not possible to reproduce the experimental data, while with the "non rigid surface models" (*i.e.*, the ER and FD models) very good agreement in particular for the TR-2PPE spectra with the experiment was achieved. These simulations confirmed earlier, rather approximate theoretical calculations, in which hydrogen like wave functions, a smaller basis set size, and ad hoc assumptions

concerning the dipole transition matrix elements were made [17]. The created superpositions of image charge states have an analog in the Rydberg wave packets or atomic physics [127]. Therefore the calculation of optimal pulses, which would lead to a "quasi classical" motion of the electron, might be a very interesting challenge for further investigations

For future work a more microscopically motivated model for the electron-electron interaction would be desirable. Also simulations for angle resolved 2PPE spectra would be most welcome. In this case one would have to include states with $\underline{k}_{\parallel} \neq 0$. Another interesting path to follow, is to simulate chemical reaction or desorption processes (see for example Ref. [12]) induced by hot electrons at surfaces. These processes are very similar to the image state dynamics studied, *i.e.*, (i) laser excitation of bulk electrons, (ii) transfer of electrons to the surface region, (iii) subsequent dynamics (coupled to nuclear motion).